nature nanotechnology

Supplementary information

https://doi.org/10.1038/s41565-025-02068-y

Exciton transport driven by spin excitations in an antiferromagnet

In the format provided by the authors and unedited

CONTENTS

S1. SUPPLEMENTARY FIGURES

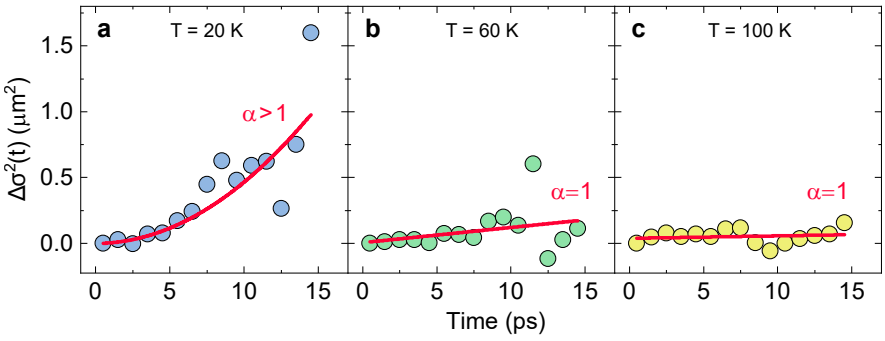

Supplementary Figure 1. **Thermal breakdown of exciton superdiffusion in 2L.** Exciton transport in 2L measured at **a** T = 20K, **b** 60K, and **c** 100K. Excitation fluence was 310 μJ/cm^2 and the transport was measured in the *b*–direction.

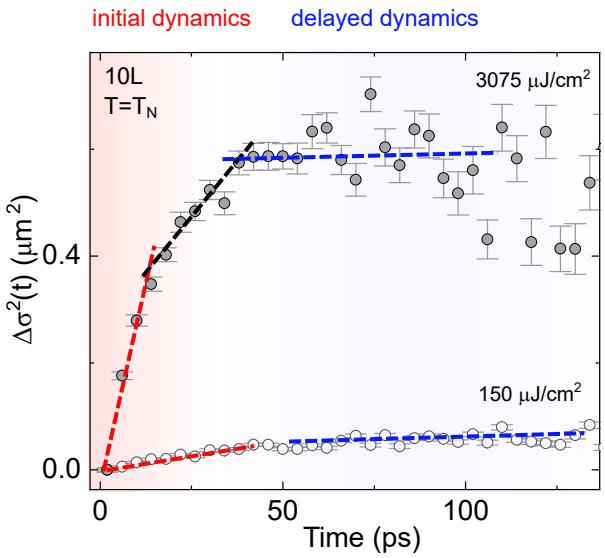

Supplementary Figure 2. **Exciton transport in 10L at $T = T_N$.** Comparison between the spatiotemporal dynamics of excitons observed at low and high excitation fluence along the b–axis. Particularly at large fluence, two distinct slopes of $\Delta\sigma(t)$ indicate distinct transport regimes labeled initial and delayed dynamics are noticeable. Error bars indicate the statistical error of the Gauss line fit.

S2. SAMPLE DETAILS

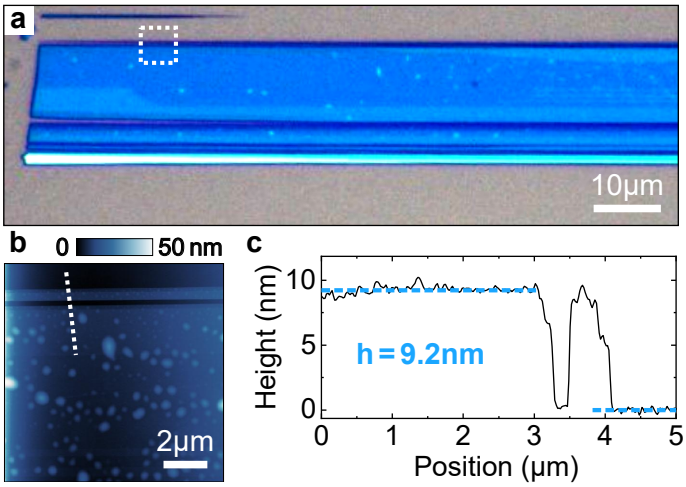

Supplementary Figure 3. **Determination of the crystal thickness.** **a** Optical microscope image of the 10L crystal. **b** Atomic force microscopy image recorded at the position marked by the white square in **a**. **c** Height profile obtained at the position indicated by the white dashed line determines a crystal thickness of $h = 9.2\,\mathrm{nm}$. Following Ref. [53] and the empirical relation $h = 0.79N + 1.12\,\mathrm{nm}$, this thickness corresponds to a layer number of $N = 10$.

S3. SPECTRAL ANALYSIS OF PL EMISSION SPECTRA UNDER INCREASING LASER EXCITATION FLUENCES

In this section we provide arguments and analysis regarding estimated photo-excited electron-hole-pair densities and compare them to the Mott density where excitons dissociate into dense electron-hole plasma. The analysis presented below suggest that excitons dominate the photo-excited density of optical quasiparticles even at the largest excitation fluences applied in our study. Strong confinement of excitons by the magnetic AFM configuration in the out-of-plane direction, as well as the large effective exciton mass ($M_a = 10.2m_0$) along the in-plane a–direction lead to excitons with very small radii and a quasi-1D density of electronic states [54]. Both render the excitons in CrSBr particularly robust against screening by free electron-hole pairs in contrast to other systems, such as semiconducting transition-metal dichalcogenides, for example.

Theoretical considerations. In our 10L crystal, under 1.61eV excitation, the largest exciton density we estimate per layer is 1.3×10^{13} cm^{-2}. Using the exciton Bohr radii (a_B^b =4.2Å along b- and a_B^a =1.3Å along a–direction) reported in a recent study [55], the approximate relation $n_M \approx 1/(\pi a_B^a a_B^b)$ leads to a Mott density of $n_M \approx 6 \times 10^{14}$ cm^{-2}. Thus, while this relation is known to slightly overestimate the Mott density, even for the largest excitation fluences used our study, exciton densities are still more than one order of magnitude below the Mott transition. For the key results presented in Fig. 1, for example, the estimated densities were substantially smaller, one the order of 10^{12} cm^{-2} per layer.

Fluence dependence in a 10L crystal. Overall, this theoretical estimate seems to be in good agreement with the fluence-dependent PL spectra measured in the 10L crystal. While we observe a broadening of the PL emission spectrum, as expected for increasing fluence, the absolute increase in linewidth is rather moderate. The PL data presented in Fig. R1 shows that the X_0 linewidth increases from 6 meV at the lowest fluence to 11 meV at the highest excitation fluence applied in our study. Even at this fluence, the X_0 exciton peak is still clearly visible and does not change its spectral shape. Moreover, we find that the integrated PL intensity of the X_0 peak increases linearly up to exciton densities as large as $\sim 5 \times 10^{12}$ cm^{-2}. As also noted above, most of the transport measurements reported in our study are conducted in this linear regime, suggesting the optical excitations are predominantly comprised of excitons. Even at larger densities, the main effect appears to be the onset of the saturation of the PL emission signal, not exciton dissociation.

Fluence dependence in a 2L crystal. It is important to note that much smaller fluences are required in order to observe pronounced transport phenomena in 2L, because exciton transport

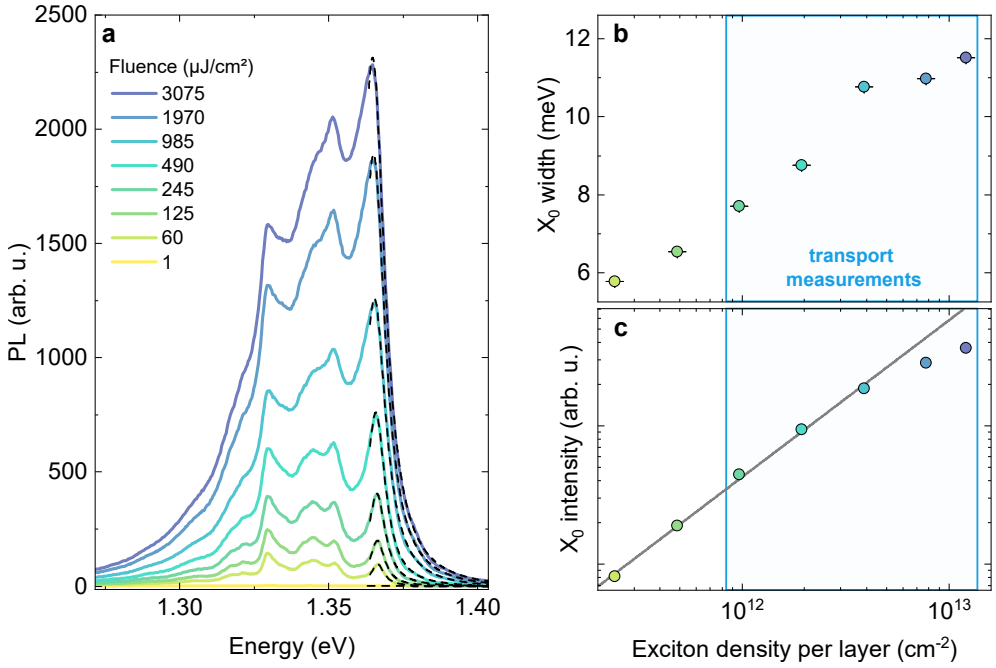

Supplementary Figure 4. Spectral analysis of the fluence-dependent PL emission at T = 4 K in the 10L crystal. **a** PL emission spectra obtained under different excitation fluences. **b** Spectral width of the X_0 exciton emission peak determined from Lorentzian fits (black dashed lines in **a**) as a function of exciton density. Error bars indicate the statistical error of the Gauss fits (dashed lines) shown in **a**. **c** Corresponding integrated intensity of the X_0 emission peak. Conversion of excitation fluence to exciton density as shown in Extended Data Fig. 2. Blue-shaded rectangles mark the regime used to study exciton transport. Laser excitation energy was set to 1.61 eV.

in these crystals is superdiffusive and exceptionally fast. Hence, our 2L transport measurements (with very few exceptions) were conducted entirely in the linear response regime. This regime is marked by the gray rectangle in Fig. R2. It is characterized by a linear scaling of the integrated PL intensity as a function of excitation fluence, consistent with the excitonic regime below the Mott transition. Moreover, we note that the linewidth of the 2L emission increases only slightly, from 14 meV to 17 meV, similar to the thicker samples. Strong screening effects that dissociate the excitons into an electron-hole plasma are therefore not expected at the fluences we used to study exciton transport also in the 2L crystals.

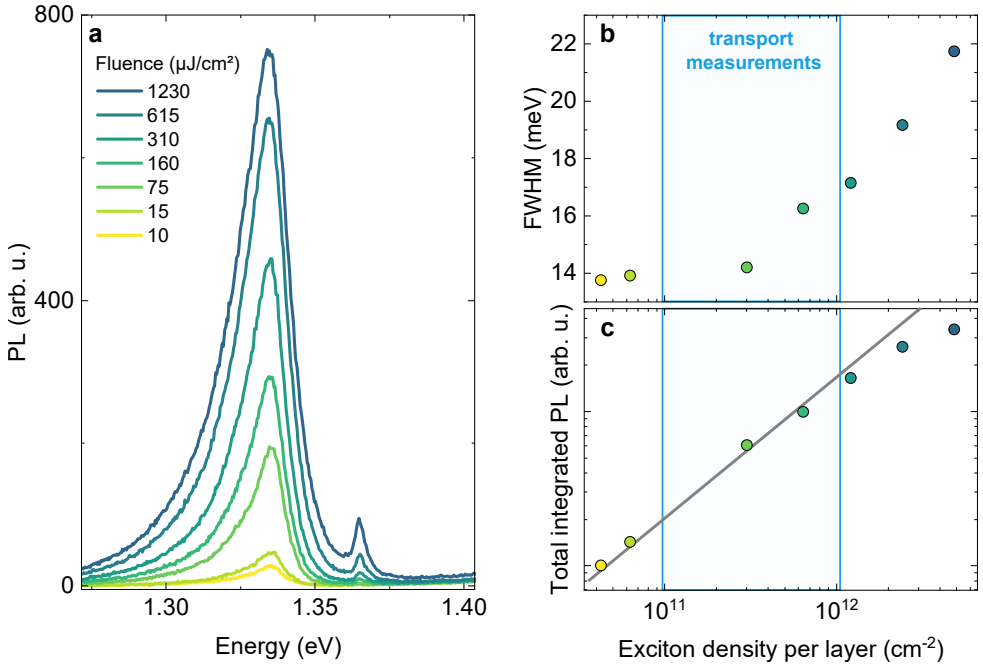

Supplementary Figure 5. Spectral analysis of the fluence-dependent PL emission in a 2L crystal at T = 4 K. a PL emission spectra obtained under different excitation fluences. **b** Full width at half maximum (FWHM) of the PL signal determined from the numerical integral as a function of the exciton density. **c** Corresponding integrated intensity of the full PL spectrum under increasing exciton densities. Blue-shaded rectangles mark the regime used to conduct the majority of 2L transport measurements. Laser excitation energy was set to 1.61 eV.

S4. DIFFERENCES IN THE OPTICAL PROPERTIES OF 2L AND 10L

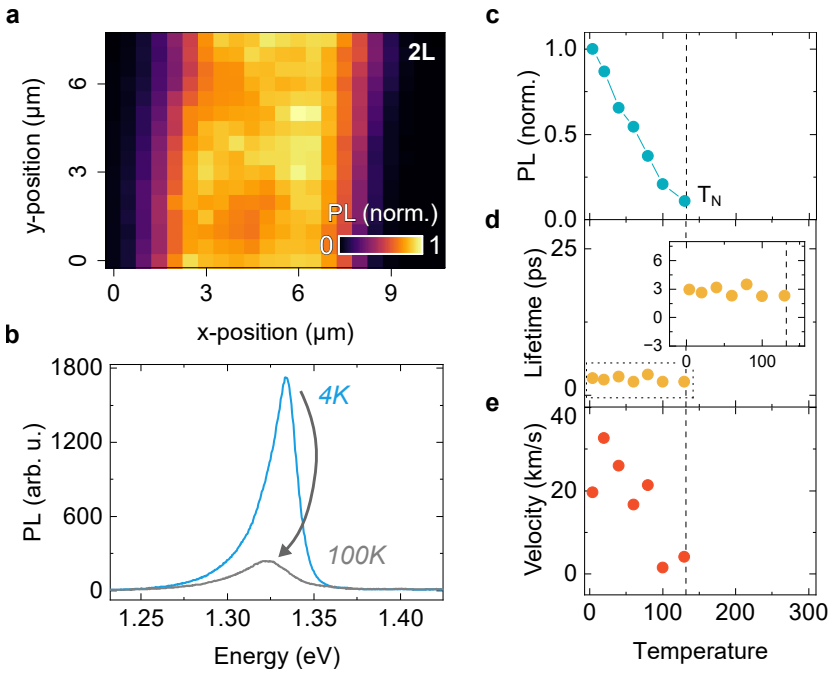

Supplementary Figure 6. **Analysis of exciton properties in a 2L. a** Spatial PL map recorded at T = 4 K. **b** Comparison between PL spectra measured at 4 K and at 100 K. **c** Integrated total PL emission as a function of temperature. **d** PL lifetime determined by a single exponential fit as a function of temperature. **e** Exciton propagation velocity as a function of temperature.

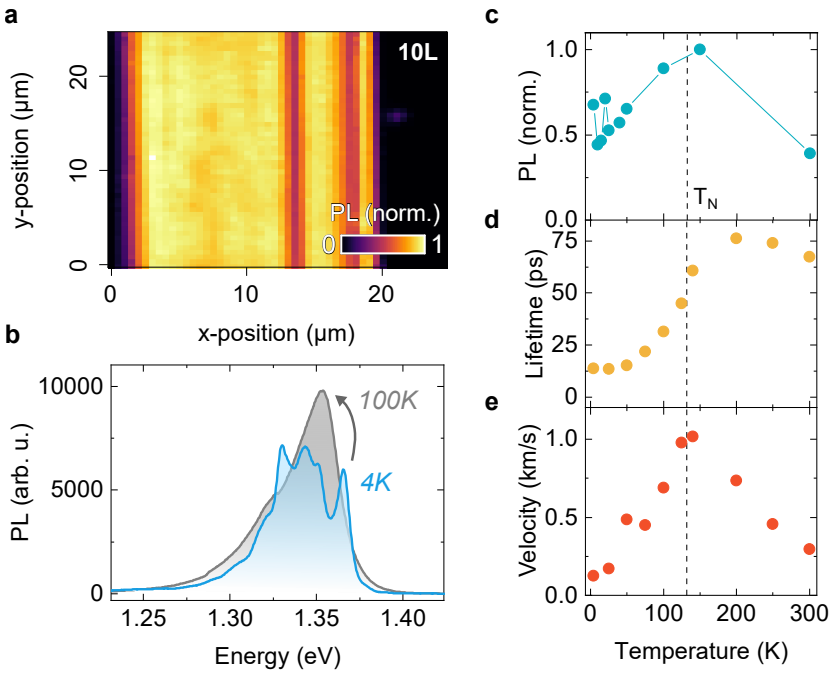

Supplementary Figure 7. **Analysis of exciton properties in a 10L. a** Spatial PL map recorded at T = 4 K. **b** Comparison between PL spectra measured at 4K and at 100K. **c** Integrated total PL emission as a function of temperature. **d** PL lifetime determined by a single exponential fit as a function of temperature. **e** Exciton propagation velocity as a function of temperature.

S5. DISCUSSION OF OTHER EXCITON TRANSPORT MECHANISMS

Here we discuss the exciton and magnon transport in CrSBr from a general theoretical standpoint. Based on the experimentally observed spatial, $\sim \mu$m, and temporal, $\sim 10 \ldots 100$ ps, scales of exciton propagation we conclude that the most appropriate description of the propagation of quasiparticles is the drift-diffusion model. It is because the spatial and temporal scales exceed microscopic lengths and times related to the mean free path, scattering time, de Broglie wavelength, etc. of excitons. We start with the linear diffusion model in Sec. S5 A, then analyze possible nonlinear effects within the excitonic system including the exciton-exciton annihilation (Auger-like effect, cf. Section S5 B), and Seebeck effect related to heating of the exciton gas (cf. Section S5 C). Then, we address the intertwined propagation of excitons and magnons in Section S7.

A. Linear exciton diffusion

The diffusion equation for the exciton density $n(\boldsymbol{r}, t)$, where $\boldsymbol{r} = (x, y)$ is the in-plane position vector and t is time, for an anisotropic van der Waals semiconductor can be written as

$$\frac{\partial n}{\partial t} + \frac{n}{\tau} = \left(D_{xx} \frac{\partial^2}{\partial x^2} + D_{yy} \frac{\partial^2}{\partial y^2} \right) n. \tag{S1}$$

Here we assumed that x and y are the principal axes in the sample plane along the crystallographic a– and b–direction, τ is the exciton lifetime related to the radiative and non-radiative recombination processes and D_{xx}, D_{yy} are the exciton diffusion coefficients. Microscopically, the diffusion coefficients are related to the velocity autocorrelation functions [56, 57] in the form

$$D_{\alpha\alpha} = \int_0^\infty \langle v_\alpha(t) v_\alpha(0) \rangle dt, \tag{S2}$$

where $\alpha = x, y$ is a Cartesian subscript and v_α is the velocity component. Based on the observed values of diffusivity we assume semiclassical exciton propagation where the autocorrelation function takes the form

$$\langle v_\alpha(t) v_\alpha(0) \rangle = \langle v_\alpha^2(0) \rangle e^{-t/\tau_s}, \tag{S3}$$

where τ_s is the scattering time and $\langle v_\alpha^2(0) \rangle = k_B T / M_\alpha$ with k_B being the Boltzmann constant, M_x and M_y being exciton translational masses along the principal axes of the structure.

As a result, for the linear diffusion coefficients we have

$$D_{xx} = \frac{k_B T}{M_x} \tau_s, \quad D_{yy} = \frac{k_B T}{M_y} \tau_s. \tag{S4}$$

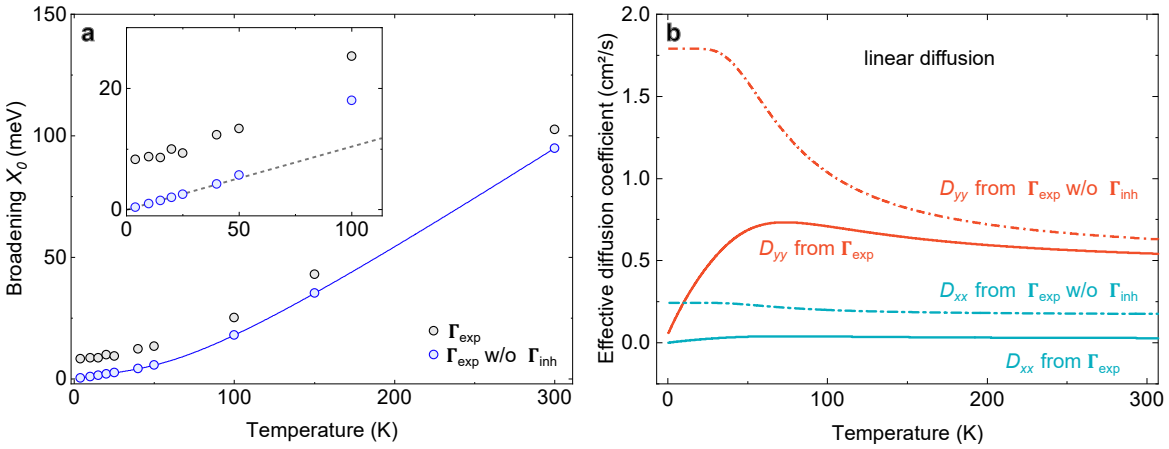

Supplementary Figure 8. Estimated temperature dependence of linear diffusion coefficients. **a** Spectral broadening of the X_0 emission peak determined from temperature-dependent PL measurements (black circles). Deconvolution removes contributions from inhomogeneous broadening Γ_{inh} (blue circles). Solid line represents the fit described in the text. Inset shows X_0 line broadening in the low-temperature range. **b** Effective diffusion coefficients estimated from Eq. (S4) for different broadening parameters Γ and crystallographic directions (a: turquoise, b: red).

This result also follows from the kinetic equation, see Sec. S5 C. Equation (S4) shows that the linear exciton diffusivity is strongly anisotropic since $M_x \neq M_y$ in CrSBr.

To obtain further insight into the linear exciton diffusion scenario we estimate the diffusion coefficients (S4) based on the bandstructure from Ref. [26] which yields $M_x = 10.2m_0$, $M_y = 0.6m_0$ and τ_s extracted following Ref. [58] from the temperature dependence of the exciton linewidth broadening Γ_{exp} assuming the relation

$$\Gamma_{exp} = \tau_s^{-1}, \tag{S5}$$

which is valid for a number of relevant scattering mechanisms, particularly in the case of long-wavelength acoustic phonon scattering.

The experimentally determined broadening is plotted in Fig. **8**a. We fit Γ_{exp} by a standard model, $\Gamma_{exp}(T) = \Gamma_0 + c_1 T + c_2/\exp\left[(E^*_{ph}/k_B T) - 1\right]$, with $c_{1,2}$ scaling parameters, Γ_0 a temperature independent parameter, and E^*_{ph} as an effective average phonon energy. The contribution $\propto c_1$ effectively accounts for the exciton interaction with long-wavelength acoustic phonons with linear dispersion and the contribution $\propto c_2$ accounts for the coupling of excitons with optical and zone edge phonons with flat dispersion. We estimate $D_{\alpha\alpha}(T)$ for two cases of the scattering time $\tau_s(T)$. First, we use $\tau_s^{-1}(T) = \Gamma_{exp}(T)$ to determine $D_{\alpha\alpha}(T)$ along a– and b–directions (solid lines in Fig. **8**b). This estimate assumes all processes contributing to $\Gamma_{exp}(0)$ involve momentum

scattering and thus impact the diffusion of excitons. Second, we consider the role of inhomogeneous broadening [58] and that momentum scattering by acoustic phonons dominates at very low temperatures. Deconvolution of $\Gamma_{exp}(T)$ with $\Gamma_{inh} = 8\,\mathrm{meV}$ renders the blue circles in Fig. **8**a. The corresponding temperature dependence of the exciton diffusion coefficient is plotted as dashed dotted lines in Fig. **8**b for transport along a– and b–directions.

B. Exciton-exciton annihilation

Diffusion Eq. (S1) assumes linear, monomolecular exciton recombination. At elevated exciton densities, bimolecular exciton recombination processes become important. In particular, exciton-exciton (X-X) annihilation where, as a result of the collision, one exciton non-radiatively recombines and the second one takes the corresponding energy and momentum [36, 59–61]. Such processes are generally described by a non-linear, quadratic recombination term [56],

$$\frac{\partial n}{\partial t} + \frac{n}{\tau} + R_A n^2 = \left(D_{xx}\frac{\partial^2}{\partial x^2} + D_{yy}\frac{\partial^2}{\partial y^2} \right) n, \tag{S6}$$

and the coefficient R_A. Following Refs. [30, 62], we obtain an increase of effective diffusion coefficients in the form

$$D^*_{\alpha\alpha} = D_{\alpha\alpha} + R_A \frac{N_0}{8\pi}, \tag{S7}$$

where the initial exciton distribution is taken in the Gaussian form

$$n(\boldsymbol{r}, 0) = \frac{N_0}{\pi r_0^2} e^{-r^2/r_0^2}, \tag{S8}$$

with N_0 being the number of injected excitons while r_0 determines the size of the excitation spot. We stress that the enhancement of $D^*_{\alpha\alpha}$ is mainly related to the modification of the shape of the exciton profile which becomes more flat at the top due to an efficient increase of the recombination rate at the spot center with the highest $n(\boldsymbol{r}, t)$. An important consequence of this result is the fact that the enhancement of the effective diffusivity is isotropic regardless of the strong anisotropy of the linear diffusion coefficients.

From our time-resolved PL measurements, we can directly estimate the impact of X-X annihilation in our experiments. Figure **10** shows the changes in the exciton decay dynamics we observe at $T = 4$, 132, and 300 K when increasing the excitation fluence. The slope of the fluence-dependent increase of the initial decay rate Γ_{int} directly determines the annihilation coefficients R_A displayed in the inset. Using these coefficients as input allows us to model the temporal evolution of $\Delta\sigma^2$ under the impact of X-X annihilation by the non-linear transport equation Eq. (S6).

In Fig. **9**a,b, we directly compare the simulated results obtained for two different exciton densities with the corresponding values of $\Delta\sigma^2$ measured in our experiments. For the simulation, we use $r_0 = \sqrt{2}\sigma_0 \approx 0.6\,\mu\text{m}$ for the width of the initial exciton distribution, which we determined by imaging the laser profile on our CCD detector. For the exciton densities, we exemplarily use $n(0,0) = 1.3 \times 10^{12}\,\text{cm}^{-2}$ and $n(0,0) = 1.3 \times 10^{13}\,\text{cm}^{-2}$, which in our experiments corresponds to an excitation fluence of $310\,\mu\text{J/cm}^2$ and $3100\,\mu\text{J/cm}^2$, respectively.

The grey diamonds plotted in Fig. **9** are obtained by imposing a linear fit onto the non-linear dynamics of the simulated $\Delta\sigma^2(t)$ values in the first 50 ps, similar to the analysis of the corresponding experimental data sets. This facilitates a meaningful comparison between the effective diffusion coefficients obtained from the simulated and the measured values of $\Delta\sigma^2(t)$.

As can be seen in Fig. **9**, the simulated values of $\Delta\sigma^2(t)$, which include the contribution from X-X annihilation, lead to a non-linear increase as a function of time. At $T = 4\,\text{K}$ and 132 K, we find a significant discrepancy between the simulated and measured values of $\Delta\sigma^2(t)$, indicating that X-X annihilation does not dominate the experimentally observed exciton transport dynamics. Moreover, the annihilation coefficient increases monotonously with temperature and does not exhibit a maximum at the Neél temperature, in particular. We thus conclude that X-X annihilation is not responsible for the signatures of exciton transport, such as the lack of in-plane anisotropy, observed in our experiments at low and moderate $\lesssim 150$ K temperatures. At $T = 300\,\text{K}$, however, good agreement between the measured and the modeled values of $\Delta\sigma^2(t)$ implies a major impact of the X-X annihilation effect on the transport dynamics of excitons measured in our experiments.

Besides the influence of X-X annihilation on exciton transport, we also note that interactions between optically created electron-hole pairs can result in their repulsion and an effective increase of the observed exciton diffusion coefficient. This effect, however, is expected to be anisotropic due to the Einstein relation between the exciton mobility and the diffusion coefficients, thus inheriting the anisotropy of $D_{\alpha\beta}$ (further discussion provided below).

Discussion of key experimental results in the context of exciton-exciton annihilation.

Exciton-exciton annihilation effects are well-known to dominate exciton diffusion coefficients in many systems under elevated excitation conditions, as was found to be the case in several earlier studies of exciton transport in monolayer transition metal dichalcogenides [30, 63, 64]. Below, we therefore discuss point by point that key exciton transport signatures in CrSBr cannot be explained by exciton-exciton annihilation effects.

1. **Maximum of D^* near the Néel temperature.** This is one of the central results of our study and a robust observation that is confirmed by measurements using two different excitation energies (at 1.61 eV, off resonance, and at 1.77 eV, in resonance with B-excitons). We find that D^* exhibits a maximum near T_N not only at large fluence but in fact across a vast range of laser excitation fluences. This maximum is even observed at the smallest fluences applied in our work (see, e.g., Extended Data Figs. 4 & 8). It cannot be explained by Auger recombination effects, since the extracted Auger rates substantially underestimate the resulting effective diffusion coefficients but also do not exhibit a maximum at the Néel temperature. Instead, they show a smooth temperature dependence, somewhat similar to that in transition metal dichalcogenides monolayers.

2. **Exciton contraction & anisotropy at low fluence.** At low temperature and for a sufficiently small fluence, we consistently observe a contraction of the exciton cloud. This phenomenon was measured in 2L, 4L, 10L & 11L thick crystals. Moreover, exciton transport is anisotropic under these conditions, because contraction is only prominently observed along the crystallographic b-direction. With respect to these observations, Auger recombination can neither account for contraction nor the resulting anisotropy, while the drag of excitons by magnons with negative group velocity may provide a reasonable explanation, as discussed in detail in Supplementary Section S7.

3. **2L superdiffusion.** The superdiffusive behavior of excitons in 2L crystals is a robust phenomenon observed in 2L sampes both with and without hBN encapsulation. In contrast, Auger recombination would lead to sub-diffusive propagation dynamics with faster initial expansion that slows down over time as the exciton density decreases. It thus does not provide an explanation for this phenomenon either.

4. **Fluence dependence & nearly isotropic transport.** These observations can result from Auger recombination. Indeed, both the fluence dependence of D^* and the observation of (nearly) isotropic transport can be signatures of Auger effects. However, even with respect to fluence dependence itself, Auger recombination quantitatively fails to account for the majority of experimental conditions explored in our study. This is especially clear for transport at the Néel temperature: Here, we observe the strongest fluence-dependence of D^* and almost isotropic exciton transport. In order to estimate whether Auger effects can be responsible for the observed effects, we analyze the changes in the initial PL decay dy-

namics induced by increasing fluence (cf. Fig. **10**). Excitation density dependent increase of the initial rate provides an independent, quantitative evaluation of the Auger recombination (see also discussion above). However, the magnitude of the effect consistently fails to explain the dependence of D^* observed along a– and b–directions by more than one order of magnitude. This strongly contrasts the results of similar analysis directly comparing density dependent recombination and diffusion in non-magnetic 2D semiconductors [30, 63]. In the case of CrSBr, to explain the experimental observation, the initial decay rate would need to be as short as one picosecond, which is clearly not within the margins of error in Fig. **10**. Similar arguments can be made for our results at low temperature ($T = 4\,\mathrm{K}$). Only at room temperature, we find that Auger effects can strongly contribute or may even determine the exciton transport observed in our experiments. For all other conditions, this is not the case.

5. **Linear fluence-dependence of PL intensity.** Lastly, we emphasize that our transport measurements are performed in a range of fluences characterized by a primarily linear PL response. This is shown in Fig. S4 for the example of our 10L crystal. Only for the largest fluence values we observe a small deviation of the PL intensity from a linear response. This provides further evidence that Auger recombination effects are not dominating the PL decay, especially at small to intermediate fluence levels.

C. Exciton Seebeck effect

Excess energy stored in the course of X-X annihilation results in local heating of excitons and thus energy gradients that can drive excitons. These gradients are inhomogeneous in space, because they are proportional to $n(\boldsymbol{r}, t)$. To analyze their impact, we consider a minimum model assuming that excitons can be described by a local temperature $T(\boldsymbol{r})$ and a local chemical potential $\mu(\boldsymbol{r})$, i.e., we assume that thermalization within the exciton ensemble is comparable to, or faster than, both the propagation timescales and the energy relaxation time (the latter describes the exchange of energy between excitons and the lattice). The temperature and chemical potential gradients result in the directed flux of excitons. To describe the effects microscopically we use the kinetic equation for the exciton distribution function $f \equiv f(\boldsymbol{k}, \boldsymbol{r}, t)$ in the form

$$\frac{\partial f}{\partial t} + \boldsymbol{v}_{\boldsymbol{k}} \cdot \frac{\partial f}{\partial \boldsymbol{r}} = Q\{f\}, \tag{S9}$$

where the exciton velocity $\boldsymbol{v}_{\boldsymbol{k}}$ is

$$\boldsymbol{v}_{\boldsymbol{k}} = \frac{1}{\hbar}\frac{\partial \varepsilon_{\boldsymbol{k}}}{\partial \boldsymbol{k}} = \left(\frac{\hbar k_x}{M_x}, \frac{\hbar k_y}{M_y}\right), \tag{S10}$$

and $\varepsilon_{\boldsymbol{k}} = \hbar^2/2(k_x^2/M_x + k_y^2/M_y)$ is the exciton dispersion. In Eq. (S9), $Q\{f\}$ is the collision integral.

We consider an exciton gas in quasi equilibrium whose chemical potential μ and temperature T are smooth (on the scale of the mean free path) functions of the coordinate. Taking the exciton distribution in the form of the quasi-equilibrium one and a small non-equilibrium correction

$$f(\boldsymbol{k}, \boldsymbol{r}, t) = \exp\left(\frac{\mu(\boldsymbol{r}) - \varepsilon_{\boldsymbol{k}}}{k_B T(\boldsymbol{r})}\right) + \delta f, \tag{S11}$$

we obtain the following equation for the non-equilibrium correction δf

$$-\boldsymbol{v}_{\boldsymbol{k}} \cdot \left(\boldsymbol{\nabla}\mu + \frac{\varepsilon_{\boldsymbol{k}} - \mu}{T}\boldsymbol{\nabla} T\right) f_0' = -\frac{\delta f}{\tau_s}, \tag{S12}$$

where f_0' is the energy derivative of the equilibrium exciton distribution function and we used the relaxation time approximation τ_s for describing exciton scattering. For an anisotropic dispersion, the scattering could be anisotropic as well, but this effect is typically weaker than the effect of the mass anisotropy on transport parameters, see, e.g., [65, 66]. It follows from Eq. (S12)

$$\delta f = \boldsymbol{v}_{\boldsymbol{k}} \cdot \left(\boldsymbol{\nabla}\mu + \frac{\varepsilon_{\boldsymbol{k}} - \mu}{T}\boldsymbol{\nabla} T\right) f_0' \tau_s, \tag{S13}$$

and the exciton flux density reads (normalization volume is set to unity)

$$\boldsymbol{i} = \sum_{\boldsymbol{k}} \boldsymbol{v}_{\boldsymbol{k}} \delta f = \sum_{\boldsymbol{k}} \boldsymbol{v}_{\boldsymbol{k}} \tau_s \left[(\boldsymbol{v}_{\boldsymbol{k}} \cdot \nabla\mu) + (\boldsymbol{v}_{\boldsymbol{k}} \cdot \boldsymbol{\nabla} T)\frac{\varepsilon_{\boldsymbol{k}} - \mu}{T}\right] f_0'. \tag{S14}$$

For non-degenerate excitons, $\mu < 0, |\mu| \gg k_B T$, Eq. (S14) can be further simplified to

$$i_\alpha = -S_{\alpha\beta}\left[-\frac{T}{\mu}\nabla_\beta \mu + \nabla_\beta T\right], \quad S_{\alpha\beta} = \frac{\mu}{T}\sum_{\boldsymbol{k}} v_{\alpha,\boldsymbol{k}} v_{\beta,\boldsymbol{k}} \tau_s f_0'. \tag{S15}$$

Here $S_{\alpha\beta}$ is the tensor of Seebeck coefficients. We recall that by definition the tensors of diffusion and Seebeck coefficients are

$$i_\alpha = -D_{\alpha\beta}\nabla_\beta n - S_{\alpha\beta}\nabla_\beta T.$$

The density of excitons is related to their chemical potential as

$$n = \frac{\sqrt{M_x M_y}}{2\pi\hbar^2} k_B T e^{\mu/k_B T} \quad \Leftrightarrow \quad \mu = k_B T \ln\left(\frac{2\pi\hbar^2 n}{k_B T\sqrt{M_x M_y}}\right), \tag{S16}$$

and the exciton compressibility is

$$\mathcal{C} = \frac{\partial n}{\partial \mu} = \frac{n}{k_B T}. \tag{S17}$$

As a result, we obtain the diffusion coefficients in the form of Eq. (S4) and Seebeck coefficients $S_{\alpha\beta} = (-\mu/T)\mathcal{C}D_{\alpha\beta}$:

$$S_{xx} = -\frac{\mu}{M_x}\frac{n}{T}\tau_s, \quad S_{yy} = -\frac{\mu}{M_y}\frac{n}{T}\tau_s. \tag{S18}$$

Note that the anisotropy of the diffusion and Seebeck coefficients is mainly inherited from the effective mass anisotropy. As a result, the enhancement of exciton propagation via the Seebeck effect is expected to be strongly anisotropic: $S_{xx}/S_{yy} \propto M_y/M_x$.

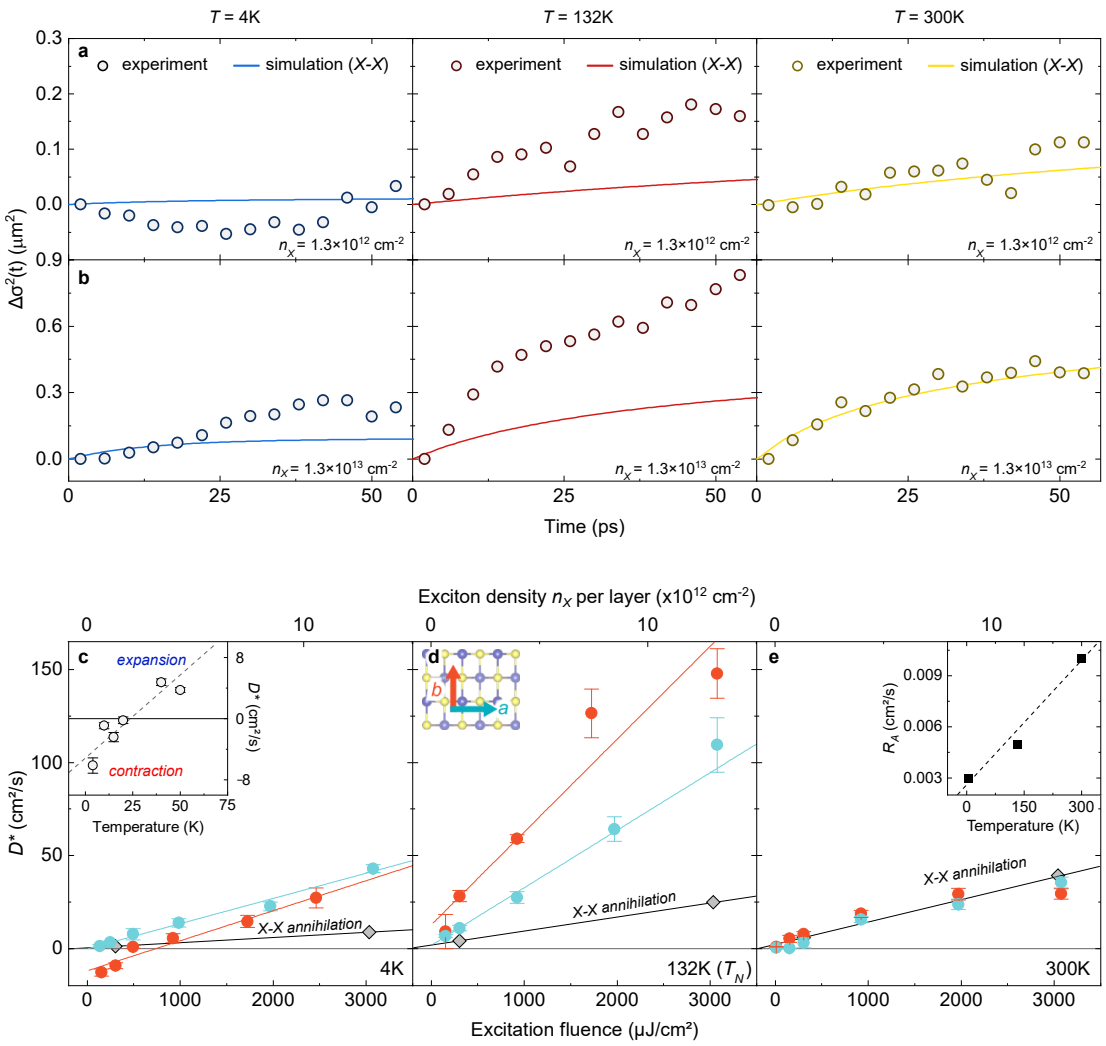

Supplementary Figure 9. **Impact of X-X annihilation on exciton transport.** Comparison between $\Delta\sigma^2(t)$ obtained from experiments and by simulating X-X annihilation effects for an excitation fluence of **a** 310 µJ/cm^2 ($n_x \approx 1.3 \times 10^{12}$ cm^2 per layer) and **b** 3100 µJ/cm^2 ($n_x \approx 1.3 \times 10^{13}$ cm^2 per layer). Data is shown for transport along the b–axis. Auger coefficients R_A used as input for the simulation are determined directly from excitation-induced changes of the initial exciton decay rate (see inset of **e** and Section 4B for details). **c-e** Fluence dependence of D^* measured for transport along a– and b–directions at 4 K, 132 K, and 300 K. Solid lines indicate linear fits. Grey diamonds and black lines represent the temperature- and density-dependent contribution of X-X annihilation effects to the measured effective diffusion coefficient D^*. Plotted values are estimates obtained from the simulation of $\Delta\sigma^2(t)$ shown in **a,b** (cf. Section 4B). Inset in **c** further shows the transition from exciton contraction to expansion under increasing sample temperatures for a fluence of 310 µJ/cm^2. We emphasize that the particular value of the transition at about 25 K is density dependent and thus does not represent any specific temperature. Error bars indicate the statistical error of the $\Delta\sigma^2(t)$ line fits.

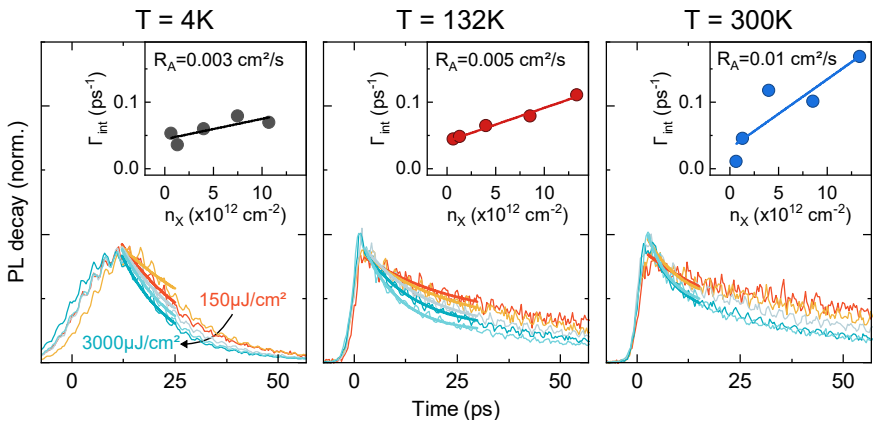

Supplementary Figure 10. **Impact of X-X recombination on exciton transport.** Exciton decay under increasing excitation fluence at $T = 4\,\mathrm{K}$, 132 K, and 300 K. Fluence-dependent changes in the initial decay rate Γ_{int} are approximated by exponential fits. Insets: Dependence of the respective initial decay rate on exciton density n_X per layer. Line represents a fit to the data, the slope of which determines the annihilation coefficient R_A.

S6. CALCULATION OF THE MAGNON DISPERSION

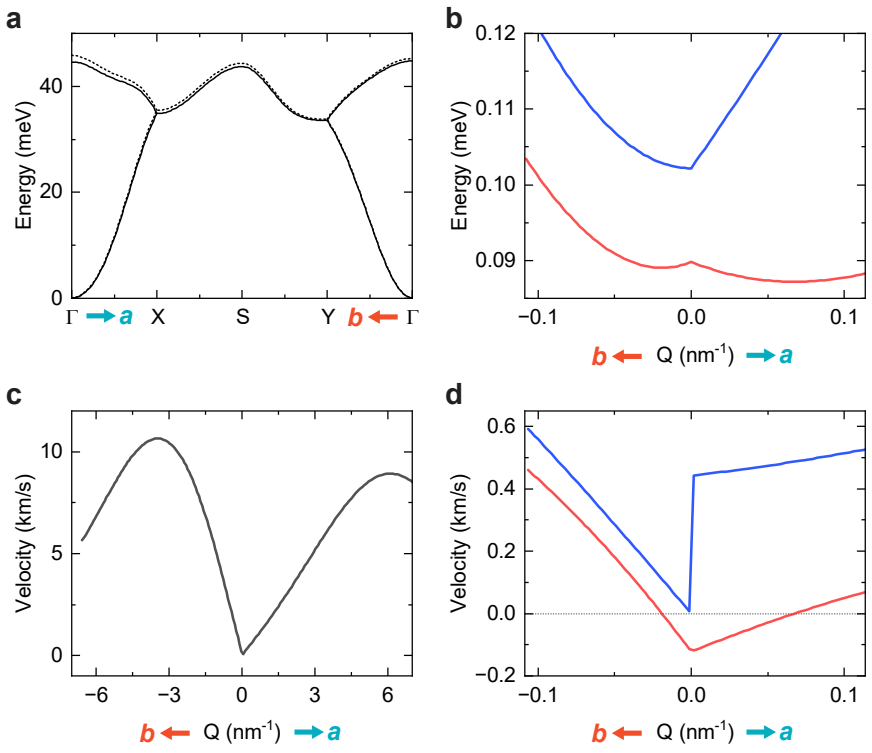

Supplementary Figure 11. Calculation of the CrSBr magnon dispersion including exchange and dipole-dipole coupling effects. a Magnon dispersion in the full Brillouin zone. Solid and dashed lines in **a** represent the two branches plotted as red and blue lines in **b**. **b** Effects of dipole-dipole coupling at small magnon momenta Q. Red and blue lines denote the two lowest branches of the dispersion. **c** Magnon velocity for large momenta in a 10L. **d** Magnon velocity for very small momenta.

A. Short-range exchange interaction and basic approach

We consider a bilayer structure for illustration of the method, but note that for a quantitative comparison with an experimental bilayer, one needs to include the impact of surface- and substrate-related changes on the magnetic properties, or other effects. The Hamiltonian of magnetic system (Cr ions) in the lattice representation consists of several contributions:

- The intralayer ferromagnetic interaction has the form

$$\mathcal{H}^{FM} = \sum_{i,j} J_{\langle ij \rangle} \left(\boldsymbol{S}_i^{(1)} \boldsymbol{S}_j^{(1)} + \boldsymbol{S}_i^{(2)} \boldsymbol{S}_j^{(2)} \right). \tag{S19}$$

Accordingly, the Fourier transform of the ferromagnetic interaction reads (the sign is selected for convenience and in accordance with our previous notes)

$$J^{FM}(\boldsymbol{k}) \equiv -\sum_{j-i} J_{\langle j-i\rangle} e^{\mathrm{i}\boldsymbol{k}\boldsymbol{r}_{j-i}}. \tag{S20}$$

Here i, j enumerate lattice sites (Cr ions), $\boldsymbol{r}_{j-i} \equiv \boldsymbol{r}_j - \boldsymbol{r}_i$. Note that the ferromagnetic interaction is isotropic.

- The interlayer exchange interaction (we consider it only for the sites one on top of the other)

$$\mathcal{H}^{AFM} = \sum_i J_{int} \boldsymbol{S}_i^{(1)} \boldsymbol{S}_i^{(2)}. \tag{S21}$$

The antiferromagnetic interaction in a reciprocal space takes the form

$$J^{AFM}(\boldsymbol{k}) \equiv -J_{int}. \tag{S22}$$

The antiferromagnetic interaction is also isotropic in the spin space.

- The contribution describes crystal anisotropy with the easy y-axis

$$\mathcal{H}^a = \sum_i A_x \left(S_{i,x}^{(1)} S_{i,x}^{(1)} + S_{i,x}^{(2)} S_{i,x}^{(2)} \right) + \sum_i A_z \left(S_{i,z}^{(1)} S_{i,z}^{(1)} + S_{i,z}^{(2)} S_{i,z}^{(2)} \right). \tag{S23}$$

In Hamiltonians above for CrSBr the dominant $J_{\langle ij\rangle} < 0$, while $J_{int} > 0$, $A_x > 0$ and $A_z > 0$. In our model in the equilibrium the spins in the first and second layers are saturated along and opposite to the y-axis.

It is convenient to introduce the coefficients

$$A_{\boldsymbol{k}} = 2SJ_{int}, \tag{S24a}$$

$$B_{\boldsymbol{k}} = 2S \left[J_{int} + A_x + A_z + J^{FM}(0) - J^{FM}(\boldsymbol{k}) \right], \tag{S24b}$$

$$C_{\boldsymbol{k}} = 2S(A_z - A_x), \tag{S24c}$$

$$D_{\boldsymbol{k}} = 0. \tag{S24d}$$

and express the eigenenergies of two splitted modes as

$$E_{\boldsymbol{k}}^{\pm} = \frac{1}{2}\sqrt{(B_{\boldsymbol{k}} \pm D_{\boldsymbol{k}})^2 - (A_{\boldsymbol{k}} \pm C_{\boldsymbol{k}})^2}. \tag{S25}$$

These expressions can be explicitly written in the form

$$E_{\boldsymbol{k}}^{+} = 2S\sqrt{\left[A_x + \frac{J^{FM}(0) - J^{FM}(\boldsymbol{k})}{2}\right]\left[J_{int} + A_z + \frac{J^{FM}(0) - J^{FM}(\boldsymbol{k})}{2}\right]}, \tag{S26a}$$

$$E_{\boldsymbol{k}}^{-} = 2S\sqrt{\left[A_z + \frac{J^{FM}(0) - J^{FM}(\boldsymbol{k})}{2}\right]\left[J_{int} + A_x + \frac{J^{FM}(0) - J^{FM}(\boldsymbol{k})}{2}\right]}. \tag{S26b}$$

Equations (S25) and (S26) are derived using the standard Holstein-Primakoff transformation introducing the Bose operators

$$S_-^{(1)} = \sqrt{2S}a^\dagger, \quad S_+^{(1)} = \sqrt{2S}a, \quad S_y^{(1)} = S - a^\dagger a,$$
$$S_x^{(1)} = \frac{1}{\mathrm{i}}\sqrt{\frac{S}{2}}(a - a^\dagger), \quad S_z^{(1)} = \sqrt{\frac{S}{2}}(a + a^\dagger), \tag{S27a}$$

$$S_-^{(2)} = \sqrt{2S}b, \quad S_+^{(2)} = \sqrt{2S}b^\dagger, \quad S_y^{(2)} = -S + b^\dagger b,$$
$$S_x^{(2)} = \frac{1}{\mathrm{i}}\sqrt{\frac{S}{2}}(b^\dagger - b), \quad S_z^{(2)} = \sqrt{\frac{S}{2}}(b + b^\dagger), \tag{S27b}$$

and applying the generalized Bogoliubov transform.

B. Dipole-dipole interaction

Now let us, in addition to the short-range exchange interaction, allow for the dipole-dipole interaction of spins. We are not interested in the effect of the dipole-dipole interactions on the ground state energy and here we study only the long-range contribution to the dispersion of magnons. Thus, for our model, it is sufficient to neglect the distance between the layers and consider a 2D lattice with the effective spins [the macroscopic approach allowing to consider multilayer bulk-like crystals is presented below in Sec. S6 C]

$$\boldsymbol{S}_i^{eff} = \boldsymbol{S}_i^{(1)} + \boldsymbol{S}_i^{(2)}. \tag{S28}$$

By virtue of Eqs. (S27) the effective spin operator can be expressed as

$$S_x^{eff} = \frac{1}{\mathrm{i}}\sqrt{\frac{S}{2}}\left(a - b - a^\dagger + b^\dagger\right), \quad S_y^{eff} = 0, \quad S_z^{eff} = \sqrt{\frac{S}{2}}\left(a + b + a^\dagger + b^\dagger\right). \tag{S29}$$

The Hamiltonian of dipole-dipole interaction between the spins has a general form [67, 68]

$$\mathcal{H}^{dd} = -\frac{\hbar^2\gamma^2}{2}\sum_{i\neq j}\frac{3\left(\boldsymbol{S}_i^{eff}\cdot(\boldsymbol{r}_j - \boldsymbol{r}_i)\right)\left(\boldsymbol{S}_j^{eff}\cdot(\boldsymbol{r}_j - \boldsymbol{r}_i)\right) - \boldsymbol{S}_i^{eff}\cdot\boldsymbol{S}_j^{eff}|\boldsymbol{r}_j - \boldsymbol{r}_i|^2}{|\boldsymbol{r}_j - \boldsymbol{r}_i|^5}, \tag{S30}$$

where $\gamma = 2\mu_B/\hbar(s/S)$ (where $s \approx 3.56/2$ [69]) is the effective gyromagnetic ratio for both layers together. The dipole-dipole interactions are important in the range of small wavevectors only, thus, at $\boldsymbol{k} \to 0$, we can treat the system as continuous. In the continuous form Hamilonian (S30) transforms to

$$\mathcal{H}^{dd} = -\frac{\hbar^2\gamma^2}{2\mathcal{A}_0^2} \times 4 \times \int d^2\boldsymbol{r}\int d^2\boldsymbol{\rho}\frac{3\left(\boldsymbol{S}^{eff}(\boldsymbol{r})\cdot\boldsymbol{\rho}\right)\left(\boldsymbol{S}^{eff}(\boldsymbol{r}+\boldsymbol{\rho})\cdot\boldsymbol{\rho}\right) - \boldsymbol{S}^{eff}(\boldsymbol{r})\cdot\boldsymbol{S}^{eff}(\boldsymbol{r}+\boldsymbol{\rho})\rho^2}{\rho^5}, \tag{S31}$$

where $\mathcal{A}_0$ is the area of the unit cell. The additional factor 4 is due to the presence of 2 Cr atoms in the plane of elementary cell.

Evaluating the integrals and assuming that the short-range contributions from the dipole-dipole interaction are included in the parameters of the basic Hamiltonian introduced in Sec. S6 A we find that the parameters $A_{\boldsymbol{k}}, \dots D_{\boldsymbol{k}}$ acquire contributions due to the dipole-dipole interaction in the form

$$A^{dd}_{\boldsymbol{k}} = -2S\hbar u \frac{k^2 - k_x^2}{k}, \tag{S32a}$$

$$B^{dd}_{\boldsymbol{k}} = -2S\hbar u \frac{k^2 - k_x^2}{k}, \tag{S32b}$$

$$C^{dd}_{\boldsymbol{k}} = -2S\hbar u \frac{k^2 + k_x^2}{k}, \tag{S32c}$$

$$D^{dd}_{\boldsymbol{k}} = -2S\hbar u \frac{k^2 + k_x^2}{k}. \tag{S32d}$$

where we introduced the constant of the dimensionality of velocity

$$u = 2\frac{\pi\hbar\gamma^2}{\mathcal{A}_0}. \tag{S33}$$

The energies of the magnons are

$$E^+_{\boldsymbol{k}} = 2S\sqrt{\left[A_x + \frac{J^{FM}(0) - J^{FM}(\boldsymbol{k})}{2}\right]\left[J_{int} + A_z + \frac{J^{FM}(0) - J^{FM}(\boldsymbol{k})}{2} - 2\hbar u k\right]}, \tag{S34a}$$

$$E^-_{\boldsymbol{k}} = 2S\sqrt{\left[A_z + \frac{J^{FM}(0) - J^{FM}(\boldsymbol{k})}{2}\right]\left[J_{int} + A_x + \frac{J^{FM}(0) - J^{FM}(\boldsymbol{k})}{2} + 2\hbar u \frac{k_x^2}{k}\right]}. \tag{S34b}$$

The branch $E^+_{\boldsymbol{k}}$ is polarized along the z-axis and the branch $E^-_{\boldsymbol{k}}$ along the x-axis. Note that the magnon velocity for the branch + at $k \to 0$ can be evaluated as

$$u_+ = -2S\sqrt{\frac{A_x}{A_z + J_{int}}}u. \tag{S35}$$

C. Macroscopic approach to the dipole-dipole interaction

1. *Magnetic susceptibility in the macroscopic approach*

We are interested at the fine structure of the magnon dispersion in the vicinity of a Γ point. To that end we consider only homogeneous (or almost) magnetization in the layers plane. Following Refs. [70–72] we present the energy density in the form

$$w = J_{int}\tilde{\mathcal{A}}_0\left(\boldsymbol{S}^{(1)} \cdot \boldsymbol{S}^{(2)}\right) - A\tilde{\mathcal{A}}_0\left[\left(\boldsymbol{S}^{(1)} \cdot \boldsymbol{n}\right)^2 + \left(\boldsymbol{S}^{(2)} \cdot \boldsymbol{n}\right)^2\right] - \hbar\gamma_1 \boldsymbol{h}\left(\boldsymbol{S}^{(1)} + \boldsymbol{S}^{(2)}\right). \tag{S36}$$

Here $\tilde{\mathcal{A}}_0 = \mathcal{A}_0/2$ is the magnetic unit cell area (area per one spin), $\boldsymbol{S}^{(i)}$ is the spin density in the layer i ($i = 1, 2$), $\gamma_1 = -\gamma$, $\boldsymbol{h}$ is the magnetic field acting on the spins. Here we use the convention that the magnetization density and the spin density are related by $\boldsymbol{M}^{(i)} = \hbar\gamma_1 \boldsymbol{S}^{(i)}$. We consider, for brevity, the axially symmetric case of $A_x = A_z \equiv A > 0$, taking into account that $\left(S_x^{(i)}\right)^2 + \left(S_y^{(i)}\right)^2 + \left(S_z^{(i)}\right)^2 = const$ we have rewritten the anisotropic term in the form of Eq. (S36) with $\boldsymbol{n} \parallel y$ being the unit vector along the y (easy) axis. The total energy $W = \int d^2 r w$.

The spin dynamics equations can be derived by variational principle in the form

$$\frac{d\boldsymbol{S}^{(i)}}{dt} + \boldsymbol{S}^{(i)} \times \boldsymbol{\Omega}_i = 0, \quad \boldsymbol{\Omega}_i = -\hbar^{-1} \frac{\delta w}{\delta \boldsymbol{S}^{(i)}}. \tag{S37}$$

Explicit calculation gives

$$\boldsymbol{\Omega}_i = -\frac{J_{int}\tilde{\mathcal{A}}_0}{\hbar} \boldsymbol{S}^{(\bar{i})} + \frac{2A\tilde{\mathcal{A}}_0}{\hbar} \boldsymbol{n}(\boldsymbol{S}^{(i)} \cdot \boldsymbol{n}) + \gamma_1 \boldsymbol{h}, \quad \bar{i} = \begin{cases} 2 \ , & i = 1, \\ 1 \ , & i = 2. \end{cases} \tag{S38}$$

In equilibrium at $\boldsymbol{h} = 0$ the magnetizations are aligned antiparallel: $\boldsymbol{S}_0^{(2)} = -\boldsymbol{S}_0^{(1)} = -S_0 \boldsymbol{n}$. In order to determine the magnetic susceptibility we need to find magnetization induced by $\boldsymbol{h}$. Let $\delta \boldsymbol{S}^{(i)} = \boldsymbol{S}^{(i)} - \boldsymbol{S}_0^{(i)}$ and let $\boldsymbol{m}_i = \hbar\gamma_1 \delta \boldsymbol{S}^{(i)} \propto \boldsymbol{h}$. Linearizing Eqs. (S37) we have

$$\frac{d\boldsymbol{m}_1}{dt} = \frac{J_{int}\tilde{\mathcal{A}}_0}{\hbar} \left[\boldsymbol{m}_1 \times \boldsymbol{S}_0^{(2)} + \boldsymbol{S}_0^{(1)} \times \boldsymbol{m}_2\right] - \frac{2A\tilde{\mathcal{A}}_0}{\hbar} \boldsymbol{m}_1 \times \boldsymbol{S}_0^{(1)} - \hbar\gamma_1^2 \boldsymbol{S}_0^{(1)} \times \boldsymbol{h}, \tag{S39a}$$

$$\frac{d\boldsymbol{m}_2}{dt} = \frac{J_{int}\tilde{\mathcal{A}}_0}{\hbar} \left[\boldsymbol{m}_2 \times \boldsymbol{S}_0^{(1)} + \boldsymbol{S}_0^{(2)} \times \boldsymbol{m}_1\right] - \frac{2A\tilde{\mathcal{A}}_0}{\hbar} \boldsymbol{m}_2 \times \boldsymbol{S}_0^{(2)} - \hbar\gamma_1^2 \boldsymbol{S}_0^{(2)} \times \boldsymbol{h}. \tag{S39b}$$

It is convenient to introduce the total magnetization density $\boldsymbol{m} = \boldsymbol{m}_1 + \boldsymbol{m}_2$ and the antiferromagnetic vector density $\boldsymbol{l} = \boldsymbol{m}_1 - \boldsymbol{m}_2$. Hence, Eqs. (S39) transform to

$$\frac{d\boldsymbol{m}}{dt} = -\frac{2A\tilde{\mathcal{A}}_0}{\hbar} \boldsymbol{l} \times \boldsymbol{S}_0^{(1)}, \tag{S40a}$$

$$\frac{d\boldsymbol{l}}{dt} = -\frac{2J_{int}\tilde{\mathcal{A}}_0}{\hbar} \boldsymbol{m} \times \boldsymbol{S}_0^{(1)} - \frac{2A\tilde{\mathcal{A}}_0}{\hbar} \boldsymbol{m} \times \boldsymbol{S}_0^{(1)} - 2\hbar\gamma_1^2 \boldsymbol{S}_0^{(1)} \times \boldsymbol{h}. \tag{S40b}$$

Combining Eqs. (S40) we obtain a single equation for $\boldsymbol{m}$ in the form

$$\frac{d^2\boldsymbol{m}}{dt^2} = \frac{2A\tilde{\mathcal{A}}_0}{\hbar} \left(\frac{2A\mathcal{A}_0}{\hbar} + \frac{2J_{int}\mathcal{A}_0}{\hbar}\right) \left[\boldsymbol{m} \times \boldsymbol{S}_0^{(1)}\right] \times \boldsymbol{S}_0^{(1)} + 4A\tilde{\mathcal{A}}_0\gamma_1^2 \left[\boldsymbol{S}_0^{(1)} \times \boldsymbol{h}\right] \times \boldsymbol{S}_0^{(1)}. \tag{S41}$$

From Eq. (S41) we obtain the magnetic susceptiblity tensor components defined by

$$m_\alpha = \chi_{\alpha\beta}^{2D} h_\beta, \quad \alpha, \beta = x, y, z, \tag{S42}$$

and $\boldsymbol{m}$ (as before) is the magnetic moment per unit area in the form

$$\chi^{2D}_{yy} = 0, \quad \chi^{2D}_{\alpha\beta} = 0 \text{ with } \alpha \neq \beta, \tag{S43a}$$

$$\chi^{2D}_{xx} = \chi^{2D}_{zz} = \frac{F}{\Omega^2 - \omega^2}, \tag{S43b}$$

and

$$\Omega^2 = \frac{4}{\hbar^2}(\tilde{\mathcal{A}}_0 S_0)^2 A(A + J_{int}), \quad F = 4A\gamma_1^2 \tilde{\mathcal{A}}_0 S_0^2 = 4A\gamma_1^2 \frac{(\tilde{\mathcal{A}}_0 S_0)^2}{\tilde{\mathcal{A}}_0}. \tag{S43c}$$

Note that $F > 0$.

Expression (S43c) for Ω (spin resonance frequency) is consistent with Eqs. (S26) (or Eqs. (S34)) at $\boldsymbol{k} = 0$ taking into account that $S = \tilde{\mathcal{A}}_0 S_0 = 3/2$:

$$E_0^{\pm} = 2S\sqrt{A(A + J_{int})} = \hbar\Omega.$$

In the vicinity of the resonance $\omega \approx \Omega$ the expressions for non-zero components of the susceptibility take the form

$$\chi^{2D}_{xx} = \chi^{2D}_{zz} \approx \frac{f}{\Omega - \omega}, \quad f = \frac{F}{2\Omega} = \gamma_1^2 \hbar \sqrt{\frac{A}{A + J_{int}}} \frac{S}{\mathcal{A}_0}. \tag{S44}$$

2. Dipole-dipole interaction via susceptibility

We use the macroscopic approach for accounting for the dipole-dipole interactions in magnetic system. To account for the dipole-dipole interactions it is sufficient to self-consistently calculate the effect of magnetic field produced by the magnetization. We focus on the relevant case of negligble retardation, $k \gg \omega/c$ where c is the speed of light, i.e., we disregard the magnons within the light cone. In this case, it is sufficient, instead of the whole set of the Maxwell equations, to solve only the magnetostatic equation

$$\operatorname{div} \boldsymbol{h}(\boldsymbol{r}, t) = -4\pi \operatorname{div} \boldsymbol{m}(\boldsymbol{r}, t), \tag{S45a}$$

with additional requirement of the curl-less field

$$\operatorname{rot} \boldsymbol{h} = 0. \tag{S45b}$$

Equation (S45b) allows us to present $\boldsymbol{h}(\boldsymbol{r}, t) = \boldsymbol{\nabla}\theta(\boldsymbol{r}, t)$ where $\theta(\boldsymbol{r}, t)$ plays a role of potential.

We have for the three-dimensional magnetization density

$$\boldsymbol{m}(\boldsymbol{k}, \omega) = \hat{\chi}^{2D}(\boldsymbol{k}, \omega)\boldsymbol{h}(\boldsymbol{k}, \omega)\delta(z), \quad \text{or} \quad m_\alpha(\boldsymbol{k}, \omega) = \chi^{2D}_{\alpha\beta}(\boldsymbol{k}, \omega) h_\beta(\boldsymbol{k}, \omega)\delta(z), \tag{S46}$$

where the Dirac δ-function accounts for the 2D nature of the studied system, $\boldsymbol{k}$ is the two-dimensional wavevector. Equation (S45a) for the potential θ takes the form

$$\frac{\partial^2\theta_{\boldsymbol{k}}(z)}{\partial z^2} - k^2\theta_{\boldsymbol{k}}(z) = 4\pi k_\alpha k_\beta \chi^{2D}_{\alpha\beta}\theta_{\boldsymbol{k}}(z)\delta(z) - 4\pi\frac{\partial}{\partial z}\delta(z)\chi^{2D}_{zz}\frac{\partial\theta_{\boldsymbol{k}}(z)}{\partial z}. \tag{S47}$$

Here we assumed that α, β are the in-plane Cartesian components (x, y), the components of the susceptibility $\chi_{\alpha,z}, \chi_{z,\alpha} \equiv 0$ and made a Fourier transform over the in-plane coordinates.

Passing to the Fourier transform along the z-axis, $\theta_{\boldsymbol{k}}(z) = \sum_q \theta_{\boldsymbol{k},q}\exp(\mathrm{i}qz)$ we have from Eq. (S47)

$$-(k^2+q^2)\theta_{\boldsymbol{k},q} = 4\pi k_\alpha k_\beta \chi^{2D}_{\alpha\beta}\sum_q \theta_{\boldsymbol{k},q} + 4\pi\chi^{2D}_{zz} q\sum_q q\theta_{\boldsymbol{k},q}. \tag{S48}$$

Summing $\theta_{\boldsymbol{k},q}$ from Eq. (S48) and $q\theta_{\boldsymbol{k},q}$ over q we obtain the equations for the eigenmodes of the system

$$1 + 2\pi\frac{k_\alpha k_\beta}{k}\chi^{2D}_{\alpha\beta} = 0, \tag{S49a}$$

and

$$1 - 2\pi k\chi^{2D}_{zz} = 0. \tag{S49b}$$

Here we have made use the following expression

$$\sum_q \frac{1}{k^2+q^2} = \frac{1}{2k}.$$

In derivation of Eq. (S49b) we have also excluded the depolarization shift by the following relation (it corresponds to the inclusion of the depolarization shift into the frequency Ω)

$$\sum_q \frac{q^2}{k^2+q^2} = \sum_q\left(1 - \frac{k^2}{k^2+q^2}\right) \to \sum_q \frac{-k^2}{k^2+q^2} = -\frac{1}{2}k. \tag{S50}$$

In-plane polarized magnon

Taking the susceptibility in the resonant form, Eq. (S44), and substituting it in Eq. (S49a) we have

$$\omega \equiv \Omega^*(\boldsymbol{k}) = \Omega + 2\pi f\frac{k_x^2}{k}, \tag{S51}$$

where we made use of the fact that $\chi_{yy} = 0$. This expression describes the dispersion of the "longitudinal" magnon in complete agreement with Eq. (S34b) at $k_x \to 0$.

Out-of-plane polarized magnon

In this case we have from Eq. (S49b) for the renormalized dispersion

$$\Omega^*(\boldsymbol{k}) = \Omega - 2\pi f k. \tag{S52a}$$

The second term provides a negative contribution to the dispersion with the speed

$$u = -2\pi f = -2S\sqrt{\frac{A}{A+J_{int}}}\frac{\pi\hbar\gamma_1^2}{\tilde{\mathcal{A}}_0} = -2S\sqrt{\frac{A}{A+J_{int}}}\frac{2\pi\hbar\gamma^2}{\mathcal{A}_0}, \tag{S52b}$$

in agreement with Eqs. (S34a) and (S35).

3. *Dipole-dipole interaction in CrSBr bulk and multilayers*

The macroscopic approach allows us to analyze the magnon dispersion for multilayer systems as well. To that end, we introduce the (bulk) magnetic susceptibility of CrSBr tensor $\hat{\chi}(\boldsymbol{k},\omega)$ and consider only small wavevectors (in the vicinity of the Γ-point of the Brillouin zone) such that there are just three independent components of the susceptibility:

$$\chi_{xx}(\boldsymbol{k},\omega) = \frac{\mathcal{F}_{xx}}{\Omega_x(\boldsymbol{k})-\omega}, \quad \chi_{zz}(\boldsymbol{k},\omega) = \frac{\mathcal{F}_{zz}}{\Omega_z(\boldsymbol{k})-\omega}, \quad \chi_{yy} = 0. \tag{S53}$$

The χ_{yy} is zero because the y-axis is the magnetization axis. The constants $\mathcal{F}_{xx}, \mathcal{F}_{zz}$ determine the coupling of the spin waves with magnetic field and $\Omega_x(\boldsymbol{k})$, $\Omega_z(\boldsymbol{k})$ are the dispersions of the spin waves found neglecting the dipole-dipole interaction.

To find the dispersion of magnons with the dipole-dipole interactions taken into account [71–73] we solve the Maxwell's equations (S45a) and (S45b). We consider a slab of CrSBr occupying the space $-L/2 < z < L/2$ with L being the slab thickness. The standard boundary conditions of continuity of tangential components of $\boldsymbol{h}$ and normal components of $\boldsymbol{b} = \boldsymbol{h} + 4\pi\boldsymbol{m}$ are imposed.

We seek the solutions of Eqs. (S45) in the form

$$\theta(\boldsymbol{r}) = \Theta(z)e^{\mathrm{i}\boldsymbol{k}\boldsymbol{r}}, \tag{S54}$$

where $\boldsymbol{k} = (k_x, k_y)$ is the in-plane wavevector. Our approach follows the procedure outlined in Ref. [51, 72].

In-plane polarized magnons

To study x-polarized magnons let us consider the frequencies $\omega \approx \Omega_x$ and assume that only χ_{xx} plays a role (the magnetization is in the plane of the slab). It follows from Eq. (S45) that

$$\frac{\partial^2\Theta(z)}{\partial z^2} - k^2\Theta(z) = \begin{cases} 4\pi k_x^2\chi_{xx}\Theta(z), & |z| < L/2, \\ 0, & |z| > L/2, \end{cases} \tag{S55}$$

where $k^2 = k_x^2 + k_y^2$. The boundary conditions are

$$\Theta(z)|_{z=\pm L/2} \text{ is continuous}, \quad \left.\frac{\partial\Theta(z)}{\partial z}\right|_{z=\pm L/2} \text{ is continuous}. \tag{S56}$$

We are looking for the lowest frequency mode only and, accordingly, seek for the solution that corresponds at $\boldsymbol{k} \to 0$ to a homogeneous magnetization. Hence,

$$\Theta(z) = \begin{cases} \cos(\tilde{k}z), & |z| < L/2, \\ \cos(\tilde{k}L/2)\exp\{[-k(|z| - L/2)]\}, & |z| > L/2, \end{cases} \tag{S57}$$

where[1]

$$\tilde{k}^2 = -k^2 - 4\pi\chi_{xx}k_x^2. \tag{S58}$$

The boundary conditions (S56) result in the equation for the eigenmodes

$$\tan\left(\frac{\tilde{k}L}{2}\right) = \frac{k}{\tilde{k}}. \tag{S59}$$

For $k \to 0$ we can find solution of Eq. (S59) analytically decomposing the left- and right-hand sides in series in small kL with the result

$$\frac{\tilde{k}L}{2} = \frac{k}{\tilde{k}} \quad \Rightarrow \tilde{k}^2 = \frac{2k}{L}.$$

Combining this expression with Eqs. (S53) and (S58) we have

$$\omega \equiv \Omega_x^*(\boldsymbol{k}) = \Omega_x(\boldsymbol{k}) + 4\pi\mathcal{F}_{xx}\frac{k_x^2}{2k/L + k^2}. \tag{S60}$$

In particular, for $k \to 0$ we obtain

$$\Omega_x^*(\boldsymbol{k}) = \Omega_x(\boldsymbol{k}) + 2\pi\mathcal{F}_{xx}L\frac{k_x^2}{k}. \tag{S61}$$

Equation (S61) demonstrates that the x-polarized magnon branch has anisotropic linear-in-$\boldsymbol{k}$ in the dispersion for small wavevectors in agreement with Eq. (S51). The factor $\mathcal{F}_{xx}L = f$ in Eqs. (S44) and (S51). The absolute value of the magnon velocity at small wavevectors increases with increase in the thickness. For large $kL \gg 1$ the magnon dispersion reaches $\Omega_x^*(\boldsymbol{k}) \approx 4\pi\mathcal{F}_{xx}$, namely, the bulk longitudinal magnon frequency. True asymptotics at $kL \to \infty$ can be derived to be

$$\Omega_x^*(\boldsymbol{k}) = \Omega_x(\boldsymbol{k}) + 4\pi\mathcal{F}_{xx}\left[1 - \left(\frac{\pi}{kL}\right)^2\right]. \tag{S62}$$

Out-of plane polarized magnons

[1] The modes we study have frequencies in the range $\Omega_\alpha(\boldsymbol{k}) \leqslant \omega \leqslant \Omega_\alpha(\boldsymbol{k}) + 4\pi\mathcal{F}_{\alpha\alpha}$ where $1 + 4\pi\chi_{\alpha\alpha}$ is negative. As a result $\tilde{k}$ is real.

Now we turn to the z-polarized magnons. To that end we consider the frequencies $\omega \approx \Omega_z$ and take into account χ_{zz} component of the susceptibility. In this way, we arrive from Eq. (S45) at

$$\frac{\partial^2\Theta(z)}{\partial z^2} - k^2\Theta(z) = \begin{cases} -4\pi\frac{\partial}{\partial z}\chi_{zz}\frac{\partial}{\partial z}\Theta(z), & |z| < L/2, \\ 0, & |z| > L/2, \end{cases} \tag{S63}$$

For z-polarized waves we have the boundary condition in the form

$$\Theta(z)|_{z=\pm L/2} \quad \text{is continuous,} \quad \frac{\partial}{\partial z}[1+4\pi\chi_{zz}]\Theta(z)\Big|_{z=\pm L/2} \quad \text{is continuous.} \tag{S64}$$

It is convenient to assume that χ_{zz} is a function of z that turns to zero outside the slab.

We look for solution where $\Theta(z)$ is an odd function of the coordinate (note that $h_z = \partial\Theta/\partial z$, hence, to have an even h_z the potential should be odd). Introducing

$$\tilde{k}^2 = -\frac{k^2}{1+4\pi\chi_{zz}}, \tag{S65}$$

we arrive at the following form of $\Theta(z)$:

$$\Theta(z) = -\begin{cases} \sin(\tilde{k}z), & |z| < L/2, \\ \operatorname{sign} z \sin(\tilde{k}L/2)\exp\{[-k(|z|-L/2)]\}, & |z| > L/2. \end{cases} \tag{S66}$$

By virtue of the boundary conditions (S64) we obtain the equation for the eigenmodes

$$\cot\left(\frac{\tilde{k}L}{2}\right) = -\frac{k}{(1+4\pi\chi_{zz})\tilde{k}}. \tag{S67}$$

Similarly to the analysis for the x-polarized modes, we consider the limit of $k \to 0$ (strictly speaking, $kL \ll 1$) and decomposing the cotangent for small argument arrive at

$$\frac{2}{L} = -\frac{k}{(1+4\pi\chi_{zz})} \quad \Rightarrow \quad 1+4\pi\chi_{zz} = -\frac{kL}{2},$$

and using Eq. (S53) we finally obtain

$$\omega \equiv \Omega_z^*(\boldsymbol{k}) = \Omega_z(\boldsymbol{k}) + 4\pi\mathcal{F}_{zz}\frac{1}{1+kL/2}. \tag{S68}$$

In particular, for $k \to 0$ we obtain

$$\Omega_z^*(\boldsymbol{k}) = \Omega_z(\boldsymbol{k}) + 4\pi\mathcal{F}_{zz} - 2\pi\mathcal{F}_{zz}Lk. \tag{S69}$$

For $kL \gg 1$ we have from Eq. (S67)

$$\Omega_z^*(\boldsymbol{k}) = \Omega_z(\boldsymbol{k}) + 4\pi\mathcal{F}_{zz}\left(\frac{\pi}{kL}\right)^2. \tag{S70}$$

Equation (S69) shows that the z-polarized magnon branch has an isotropic k-linear contribution to the dispersion with *negative* slope. Equation (S69) is in agreement with Eqs. (S35) and (S52).

Naturally, for $kL \ll 1$ the system is essentially two-dimensional and the dispersion is linear in the k. The propagation velocity linearly increases with the thickness L, but the range of validity of linear dispersion shrinks with increase in the thickness. The relation between the bulk and two-dimensional susceptibilities is basically the same as for the dielectric susceptibilities in two-dimensional transition metal dichalcogenides:

$$\chi^{2D}_{\alpha\beta} = \chi^{3D}_{\alpha\beta} L. \tag{S71}$$

Note that this expression is approximate for actual bilayer or four-layer CrSBr samples due to atomistic effects and in that case the magnetic response of a few layer CrSBr is more rigorously described within a two-dimensional model (S46).

S7. MAGNON-EXCITON DRAG EFFECT

We turn now towards discussing the coupled propagation of excitons and magnons. As outlined in the main manuscript, we assume that the optical excitation of the sample generates both excitons and magnons. These quasiparticle ensembles form a two-component system with mutual drag caused by the interactions of excitons and magnons. Below we discuss basic scenarios of the magnon-exciton drag effect within a semi-phenomenological model.[2]

A. Exciton-magnon interaction

Microscopically, the exciton-magnon interaction can be easily understood for a two-layer case where canting of spins in the two magnetic sublattices with spins $\boldsymbol{S}^{(1)}$ and $\boldsymbol{S}^{(2)}$ results in the variation of the exciton energy, e.g., due to electron and hole interlayer tunneling in the canted configuration. In this case, intralayer excitons become mixed with the interlayer ones and their energy decreases. We present the exciton energy variation as a function of layer magnetization in the form (cf. Refs. [4, 7, 8]):

$$V = \Xi \int d\boldsymbol{r} \mathcal{X}^\dagger(\boldsymbol{r}) \mathcal{X}(\boldsymbol{r}) \left[S^2 + \boldsymbol{S}^{(1)}(\boldsymbol{r}) \cdot \boldsymbol{S}^{(2)}(\boldsymbol{r}) \right], \tag{S72}$$

which is related to a local coupling of the intralayer exciton with the higher-in-energy interlayer one. In Eq. (S72), $\Xi \equiv \Xi(S) < 0$ is the parameter, and $\mathcal{X}^\dagger$, $\mathcal{X}$ are the exciton creation and annihilation operators. The combination is

$$S^2 + \boldsymbol{S}^{(1)}(\boldsymbol{r}) \cdot \boldsymbol{S}^{(2)}(\boldsymbol{r}) = 2S^2 \cos^2(\theta/2), \tag{S73}$$

where θ is the angle between the vectors $\boldsymbol{S}^{(1)}$ and $\boldsymbol{S}^{(2)}$. Equation (S72) demonstrates the reduction of the exciton energy for $\Xi < 0$ if the magnetizations in the layers are canted with respect to their equilibrium $\boldsymbol{S}^{(1)} = -\boldsymbol{S}^{(2)} = S\hat{\boldsymbol{y}}$ orientations.

It is convenient to introduce

$$S_\pm^{(1,2)} = S_z^{(1,2)} \pm \mathrm{i} S_x^{(1,2)}, \tag{S74}$$

obeying the commutation relations

$$S_+^{(1,2)} S_-^{(1,2)} - S_-^{(1,2)} S_+^{(1,2)} = 2S_y^{(1,2)}, \quad S_y^{(1,2)} S_\pm^{(1,2)} - S_\pm^{(1,2)} S_y^{(1,2)} = \pm S_\pm^{(1,2)}. \tag{S75}$$

[2] A detailed theory of the magnon-exciton interactions and drag based on the microscopic Hamiltonian and kinetic equation will be presented elsewhere.

Let $S_y^{(1)} = -S_y^{(2)} \equiv S > 0$ (antiferromagnetic configuration at saturation). In the case of classically large spin we can use the Holstein-Primakoff transformation [70] and present the spin operators in the approximate form

$$S_-^{(1)} = \sqrt{2S}a^\dagger, \quad S_+^{(1)} = \sqrt{2S}a, \quad S_y^{(1)} = S - a^\dagger a, \quad S_x^{(1)} = \frac{1}{\mathrm{i}}\sqrt{\frac{S}{2}}(a - a^\dagger), \quad S_z^{(1)} = \sqrt{\frac{S}{2}}(a + a^\dagger), \tag{S76a}$$

$$S_-^{(2)} = \sqrt{2S}b, \quad S_+^{(2)} = \sqrt{2S}b^\dagger, \quad S_y^{(2)} = -S + b^\dagger b, \quad S_x^{(2)} = \frac{1}{\mathrm{i}}\sqrt{\frac{S}{2}}(b^\dagger - b), \quad S_z^{(2)} = \sqrt{\frac{S}{2}}(b + b^\dagger), \tag{S76b}$$

via bosonic operators a, $a^\dagger$, b, $b^\dagger$. Making use of Eq. (S76), we obtain (keeping only the lowest powers of the a and b operators)

$$V = \Xi S \int d\boldsymbol{r} \mathcal{X}^\dagger(\boldsymbol{r})\mathcal{X}(\boldsymbol{r}) \left[a^\dagger(\boldsymbol{r})a(\boldsymbol{r}) + b^\dagger(\boldsymbol{r})b(\boldsymbol{r}) + a^\dagger(\boldsymbol{r})b^\dagger(\boldsymbol{r}) + a(\boldsymbol{r})b(\boldsymbol{r})\right]. \tag{S77}$$

Operators a, $a^\dagger$, b, $b^\dagger$ are linearly related (via the Bogoliubov transform) with the magnon creation and annihilation operators. Thus, Eq. (S72) shows that only two-magnon processes are of importance: exciton can be scattered by the magnon or can emit or absorb two magnons simultaneously.

To obtain deeper insight into this two-magnon-exciton interaction, let us analyze the exciton-magnon interaction from the symmetry standpoint. We focus on the coupling between a non-degenerate optically active exciton state (allowed in y polarization) that transforms according to the B_{2u} or Γ_2^- irreducible representation of the D_{2h} point group. The effective Hamiltonian of exciton-magnon interaction should be invariant under all point-group transformations. Since $B_{2u} \times B_{2u} = A_g$ (or Γ_1^+, identity representation) the only components or combinations of components of magnetization that enter the coupling Hamiltonian should be invariant. In our case it is S_y, S_y^2, S_x^2, S_z^2, ... (in each layer the magnetization is either parallel or antiparallel to the easy-y-axis, thus S_y is invariant). These combinations are quadratic in the magnon operators, thus only two-magnon processes are possible at zero external magnetic field in agreement with the microscopic analysis presented above.

B. Two component exciton-magnon drift-diffusion

Under the same assumptions as in Section S5 A, let us derive phenomenological equations describing the propagation of excitons and magnons. Introducing $m(\boldsymbol{r}, t)$, the magnon density[3],

[3] Here, for simplicity, we sum over all magnon branches.

we obtain, assuming its smooth variation in space and time, the set of continuity equations for magnons and excitons

$$\frac{\partial m}{\partial t} + \boldsymbol{\nabla} \cdot \boldsymbol{j} + R_m\{m\} = G_m, \tag{S78a}$$

$$\frac{\partial n}{\partial t} + \boldsymbol{\nabla} \cdot \boldsymbol{i} + R_x\{n\} = G_x. \tag{S78b}$$

Here $\boldsymbol{j}$ and $\boldsymbol{i}$ are the magnon and exciton fluxes, G_m and G_x the magnon and exciton generation rates, respectively, $R_m\{m\}$ and $R_x\{n\}$ are the operators describing relaxation of the quasiparticles, e.g., $R_x\{n\} = n/\tau + R_A n^2$ describing monomolecular and bimolecular recombination of excitons.

Within the drift-diffusion approach, the fluxes should be related to the density gradients and interparticle drag forces related to exciton-magnon interaction. We focus here on the exciton flux and present it in the form

$$\boldsymbol{i} = \boldsymbol{i}_{\text{diff}} + \boldsymbol{i}_{\text{dr}}, \tag{S79}$$

via the diffusive $i_{\text{diff},\alpha} = -D_{\alpha\beta}\partial n/\partial x_\beta$ and $\boldsymbol{i}_{\text{dr}}$ components. We recast the drift contribution as

$$\boldsymbol{i}_{\text{dr}} = n\boldsymbol{v}, \tag{S80}$$

where $\boldsymbol{v}$ is the exciton drift velocity determined as an average over the exciton ensemble

$$\boldsymbol{v} = \sum_{\boldsymbol{k}} \boldsymbol{v}_{\boldsymbol{k}} f_{\boldsymbol{k}}, \tag{S81}$$

in terms of a non-equilibrium distribution function of excitons $f_{\boldsymbol{k}}$. Similarly, the drift flux of magnons reads

$$\boldsymbol{j}_{\text{dr}} = m\boldsymbol{u}, \tag{S82}$$

where $\boldsymbol{u}$ is the magnon drift velocity.

Due to the exciton-magnon interaction the exciton and magnon velocities are coupled as

$$\frac{dv_\alpha}{dt} + \Gamma^0_{\alpha\beta} v_\beta + \Gamma^m_{\alpha\beta}(v_\beta - u_\beta) = M^{-1}_{\alpha\beta} F_\beta. \tag{S83}$$

Here $\Gamma^0_{\alpha\beta}$ is the exciton momentum relaxation rates tensor unrelated to the exciton-magnon scattering (due to phonons, disorder, etc.) and $\Gamma^m_{\alpha\beta}$ is the tensor of exciton-magnon scattering rates. The rates $\Gamma^m_{\alpha\beta}$ can depend on the excitation power due to magnon population. In Eq. (S83), $\boldsymbol{F}$ is the external force acting on the excitons (due to the Seebeck effect of excitons, exciton-exciton repulsion[4] or phonon drag/wind), see Refs. [40–42, 74–77] for details.

[4] In the presence of effective exciton-exciton repulsion $\boldsymbol{F} \propto \boldsymbol{\nabla} n$ and effective diffusion coefficient is enhanced. However, this enhancement is anisotropic due to inverse effective mass factor in the right hand side of Eq. (S30), see also Sec. S5 and Refs. [1,7] for details.

Assuming that $\boldsymbol{F} = 0$ and that x and y are the principal axes of the structure, we have in the steady state

$$v_\alpha = u_\alpha \frac{\Gamma^m_{\alpha\alpha}}{\Gamma^0_{\alpha\alpha} + \Gamma^m_{\alpha\alpha}}, \quad \alpha = x \ \text{ or } \ y. \tag{S84}$$

At $\Gamma^m \ll \Gamma^0$ (conventional, linear drag regimes), the exciton velocity $v \ll u$. In this case only a small fraction of magnon momentum is transferred to excitons. At $\Gamma^m \gg \Gamma^0$ (a lot of magnons, highly nonlinear regime) the exciton velocity saturates at $\boldsymbol{u}$ irrespectively of its direction. Thus, the propagation speed of excitons is limited by the magnon speed.

Equation (S84) is the central result of our model. It allows to understand key features of the exciton propagation in few-layer CrSBr:

1. Fast exciton propagation with effective diffusion coefficients exceeding by far the estimates based on the exciton linear diffusion model in Sec. S5 A. Indeed, we assume that for a wide range of excitation powers used in experiment the magnon occupancies are high and exciton-magnon scattering dominates over the exciton momentum relaxation related to phonon and disorder scattering:

   $$\Gamma^m \gtrsim \Gamma^0. \tag{S85}$$

   In that case exciton propagation velocities are close to those of magnons. The exciton transport velocities ($\sim$km/s) observed in our experiment are in overall good agreement with the transport velocities of magnons reported in recent studies [7].

2. Maximum of the effective exciton diffusion coefficient in the vicinity of the Néel temperature T_N: An increase in the magnon occupancies as the temperature T approaches T_N results in the increase of Γ^m. As a result, the effective diffusion coefficient of excitons should have a maximum at $T \approx T_N$.

3. Almost isotropic exciton propagation: Under condition (S85), the excitons co-propagate with magnons whose dispersion is just weakly anisotropic in contrast to that of excitons (cf. Refs. [7] and [26]). Hence, the magnon cloud expands virtually isotropically and due to exciton-magnon interactions, the expansion of the exciton cloud follows the magnon cloud expansion.

C. Contraction of the exciton cloud

We briefly discuss two mechanisms potentially responsible for the contraction of excitons observed in our measurements at low temperature and under low excitation fluence (see, for example, Fig. 3 of the main manuscript). In the first mechanism, we consider that optical excitation may locally create a transient, attractive potential for excitons which leads to exciton funneling, an effect that would be observed as negative transport (contraction) in our experiments. From a comparison with our numerical model, however, we conclude that the intrinsic diffusion coefficients required in this model to match our experimental results are unreasonable. We therefore also consider that the negative group velocity of low-frequency, Γ-point magnons in CrSBr reported in a recent study [21] could lead to a negative magnon-exciton drag effect.

1. *Excitation-induced transient attractive potential*

With the drift-diffusion model, we estimate the transport of excitons in the presence of an attractive, excitation-induced transient potential. Such a potential may in principle be created by the distortion of the magnetic order in the region of optical excitation, as is discussed in the main text in the context of Fig. 2. It is important to note, however, that negative transport of excitons is only observed under low excitation fluence. The density of thermal fluctuations (incoherent magnons) induced in this case are therefore small. Nonetheless, they may lead to a local minimum in the exciton energy landscape. From optical spectroscopy, however, we can conclude that the depth of this potential cannot be more than ≈ -1 meV; otherwise, it would lead to notable spectral shifts of the exciton emission peak in the upper panel of Fig. 2c of the main manuscript.

We therefore model exciton transport by including in the left-hand side of kinetic Eq. (S9) the force term

$$\frac{\boldsymbol{F}}{\hbar}\cdot\frac{\partial f}{\partial \boldsymbol{k}}, \quad \text{where} \quad \boldsymbol{F}=-\boldsymbol{\nabla}V(\boldsymbol{r},t), \tag{S86}$$

where $V(\boldsymbol{r},t)$ is the attractive potential produced by the magnon cloud. As a result, the diffusion Eq. (S1) takes the form

$$\frac{\partial n}{\partial t}+\frac{n}{\tau_r}=\sum_{\alpha,\beta}D_{\alpha\beta}\left[\frac{\partial^2}{\partial x_\alpha x_\beta}n+\frac{1}{k_BT}\frac{\partial}{\partial x_\alpha}n\frac{\partial V}{\partial x_\beta}\right]. \tag{S87}$$

Figure **12**b shows the results of a simulation of exciton transport within this model with

$$V(\boldsymbol{r},t)=-V_0\exp\left(-\frac{r^2}{r_0^2}-\frac{t}{\tau_\varepsilon}\right), \tag{S88}$$

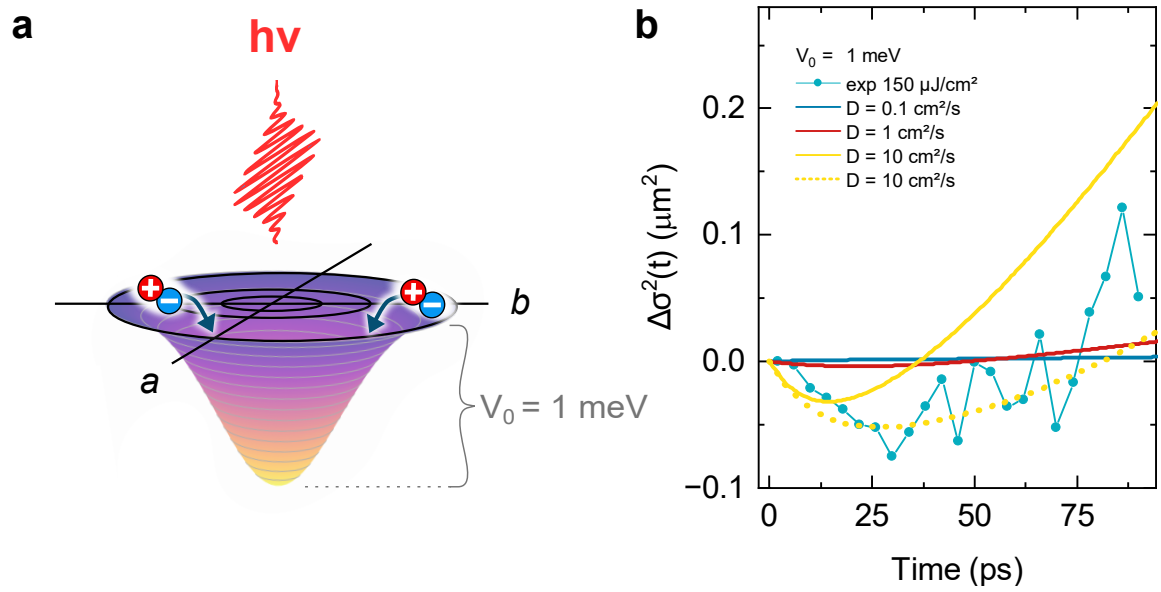

Supplementary Figure 12. Simulation of exciton transport dynamics in the presence of an attractive potential. a Sketch of the attractive potential considered in the model. Spectral analysis of the X_0 emission peak limits the depth of the potential to $V_0 \approx 1$ meV. **b** Calculated time evolution of $\Delta\sigma^2$ for different values of the exciton diffusion coefficient D. Depth of the potential used in the simulations is V_0=1 meV, the exciton lifetime is τ=15 ps, and T=5 K. The decay constant of the potential is $\tau_\varepsilon = 2\tau$ for all curves except for the yellow dashed line ($\tau_\varepsilon = 6\tau$). Blue dots and line represent $\Delta\sigma^2$ values measured in a 10L crystal under 155 μJ/cm^2.

where r_0 is the excitation spot size [cf. Eq. (S8)], $V_0 > 0$ is the depth of the potential well created by the magnons, and τ_ε is the decay time of this potential. It is seen from Fig. **12**b that to describe the dynamics of $\Delta\sigma^2(t)$ for a reasonable depth of the potential well and realistic values of temperature, the diffusion coefficient should significantly exceed the value estimated on the basis of the linewidths.

2. Negative magnon group velocity and exciton-magnon drag

Another possible scenario for the contraction of the exciton cloud is related to the specifics of the magnon dispersion in CrSBr in the region of small wavevectors $k \lesssim 1$ μm^{-1}, which are the result of dipole-dipole interaction in the spin system. Indeed, as demonstrated theoretically and experimentally [21] the group velocity of one of the magnon branches becomes negative or, strictly speaking, the group and phase velocities become antiparallel (see Fig. **11** and also Fig. 3b

of Ref. [21]):

$$\boldsymbol{v}_{g,-} = \frac{\partial \omega_-(\boldsymbol{k})}{\partial \boldsymbol{k}} \uparrow\downarrow \boldsymbol{k}. \tag{S89}$$

As a result, two effects become possible

1. The non-equilibrium magnon can contract, since magnons with negative group velocity can propagate towards the density gradient in contrast to the equilibrium diffusion where the particles propagate against the density gradient.

2. The direction of exciton drag can be opposite to the direction of the magnon propagation as a result of the negative magnon dispersion in the energy and momentum conservation laws underlying exciton magnon collisions.

Below we present a model which demonstrates that the exciton drag can be opposite to the direction of magnon propagation (scenario 2 above).

3. Kinetic approach to exciton contraction

We present the kinetic equation (S9) for the exciton distribution function in the form

$$\frac{\partial f}{\partial t} + \boldsymbol{v}_{\boldsymbol{k}} \frac{\partial f}{\partial \boldsymbol{r}} = Q^0\{f\} + Q^m\{f, m\}, \tag{S90}$$

where we explicitly separated the collision integral in two contributions $Q^0\{f\}$ and $Q^m\{f, m\}$ that describe exciton scattering by static disorder/phonons and by magnons, respectively. Hereafter we omit all irrelevant arguments of the distribution function for brevity.

In the case of exciton-magnon scattering (2 magnon processes) the collision integral describing the process

$$\text{exciton } \boldsymbol{k} + \text{ magnon } \boldsymbol{p} \to \text{exciton } \boldsymbol{k}+\boldsymbol{q} + \text{ magnon } \boldsymbol{p}-\boldsymbol{q},$$

where $\boldsymbol{q}$ is the transferred wavevector, reads

$$Q^m\{f, m\} = \sum_{\boldsymbol{q},\boldsymbol{p}} \frac{2\pi}{\hbar} |M(\boldsymbol{k}, \boldsymbol{p}; \boldsymbol{q})|^2 \delta(\varepsilon_{\boldsymbol{k}} + E_{\boldsymbol{p}} - \varepsilon_{\boldsymbol{k}+\boldsymbol{q}} - E_{\boldsymbol{p}-\boldsymbol{q}})$$
$$\times \{f(\boldsymbol{k}+\boldsymbol{q})[1+f(\boldsymbol{k})] m_{\boldsymbol{p}-\boldsymbol{q}}[1+m_{\boldsymbol{p}}] - f(\boldsymbol{k})[1+f(\boldsymbol{k}+\boldsymbol{q})] m_{\boldsymbol{p}}[1+m_{\boldsymbol{p}-\boldsymbol{q}}]\}. \tag{S91}$$

Here $M(\boldsymbol{k}, \boldsymbol{p}; \boldsymbol{q})$ is the appropriate matrix element, $\varepsilon_{\boldsymbol{k}}$ is the exciton dispersion, $E_{\boldsymbol{p}}$ is the magnon dispersion [for simplicity we consider only one branch], $m_{\boldsymbol{p}}$ is the (nonequilibrium) magnon distribution function. Equation (S91) accouts for the processes where exciton with the wavevector $\boldsymbol{k}$

and magnon with the wavevector $\boldsymbol{p}$ scatter each other and, as a result, exciton arrives at the state with the wavevector $\boldsymbol{k}+\boldsymbol{q}$ and magnon to the state $\boldsymbol{p}-\boldsymbol{q}$ (and the reverse process), where $\boldsymbol{q}$ is the scattering wavevector.

We neglect exciton exciton collisions and assume that the magnon distribution function $m_{\boldsymbol{p}}$ ($\boldsymbol{p}$ is the magnon wavevector) is in the form

$$m_{\boldsymbol{p}} = m_0(E_{\boldsymbol{p}}) + m_0'(E_{\boldsymbol{p}})\tau_m(\boldsymbol{V_p}\boldsymbol{\nabla}\mu_m). \tag{S92}$$

Here, the first term, $m_0(E_p)$, is the isotropic quasi-equilibrium magnon distribution function, and the second term represents the non-equilibrium contribution related to the magnon propagation, τ_m is the magnon relaxation time, μ_m is the magnon chemical potential, and $\boldsymbol{V_p} = \hbar^{-1}\partial E_{\boldsymbol{p}}/\partial \boldsymbol{p}$ is the magnon velocity. We use the notation $m_0'(E_{\boldsymbol{p}}) = dm_0/dE_{\boldsymbol{p}}$. Note that the total magnon velocity described by the distribution function (S92)

$$\boldsymbol{u} = \frac{\sum_{\boldsymbol{p}} \boldsymbol{V_p} m_0'(E_{\boldsymbol{p}})\tau_m(\boldsymbol{V_p}\boldsymbol{\nabla}\mu_m)}{\sum_{\boldsymbol{p}} m_0(E_{\boldsymbol{p}})} = \tau_m \frac{\boldsymbol{\nabla}\mu}{2}\frac{\sum_{\boldsymbol{p}} V_{\boldsymbol{p}}^2 m_0'(E_{\boldsymbol{p}})}{\sum_{\boldsymbol{p}} m_0(E_{\boldsymbol{p}})} \uparrow\downarrow \boldsymbol{\nabla}\mu. \tag{S93}$$

The magnon flux is counter to the gradient of chemical potential, as expected ($m_0' < 0$ for equilibrium distribution) regardless the sign of the magnon dispersion.

Linearizing the collision integrals and solving the kinetic equation we arrive at

$$\delta f(\boldsymbol{k}) = \tau_p \times \frac{2\pi}{\hbar} f_0'(\varepsilon_{\boldsymbol{k}}) \sum_{\boldsymbol{p},\boldsymbol{q}} |M(\boldsymbol{k},\boldsymbol{p};\boldsymbol{q})|^2 \delta(\varepsilon_{\boldsymbol{k}} + E_{\boldsymbol{p}} - \varepsilon_{\boldsymbol{k}+\boldsymbol{q}} - E_{\boldsymbol{p}-\boldsymbol{q}}) m_0(E_{\boldsymbol{p}}) \times \tau_m \left[(\boldsymbol{V_{p-q}} - \boldsymbol{V_p})\cdot\boldsymbol{\nabla}\mu_m\right], \tag{S94}$$

where as above we assumed that the occupancies of the states are small, $f_0'(\varepsilon_{\boldsymbol{k}}) = df_0/d\varepsilon$ and τ_p is the exciton momentum relaxation time contributed both by exciton-magnon and exciton-phonon/disorder collisions [cf. Eq. (S83)]

$$\frac{1}{\tau_p} = \Gamma^0 + \Gamma^m.$$

Hereafter we assume either isotropic approximation or one-dimensional propagation, that is why the subscripts α and β are omitted.

Neglecting the magnon dispersion compared to the exciton dispersion in the energy conservation δ-function, changing the summation variable from $\boldsymbol{q}$ to $\boldsymbol{k}' = \boldsymbol{k}+\boldsymbol{q}$ and assuming isotropy in the plane or one-dimensional propagation we have

$$\delta f(\boldsymbol{k}) = \tau_p \times \frac{2\pi}{\hbar} f_0'(\varepsilon_{\boldsymbol{k}}) \sum_{\boldsymbol{p},\boldsymbol{k}'} |M(\boldsymbol{k},\boldsymbol{p};\boldsymbol{k}'-\boldsymbol{k})|^2 \delta(\varepsilon_{\boldsymbol{k}} - \varepsilon_{\boldsymbol{k}'}) m_0(E_{\boldsymbol{p}}) \left(\boldsymbol{V_{p+k-k'}}\cdot\boldsymbol{\nabla}\mu_m\tau_m\right). \tag{S95}$$

The excitons drift with the velocity

$$\boldsymbol{v} = \frac{1}{\sum_{\boldsymbol{k}} f_0(\varepsilon_{\boldsymbol{k}})} \sum_{\boldsymbol{k}} \frac{1}{\hbar} \frac{\partial \varepsilon_{\boldsymbol{k}}}{\partial \boldsymbol{k}} \delta f(\boldsymbol{k})$$
$$= \tau_p \frac{2\pi}{\hbar} \sum_{\boldsymbol{p},\boldsymbol{k},\boldsymbol{k}'} f_0'(\varepsilon_{\boldsymbol{k}}) |M(\boldsymbol{k},\boldsymbol{p};\boldsymbol{k}'-\boldsymbol{k})|^2 \delta(\varepsilon_{\boldsymbol{k}} - \varepsilon_{\boldsymbol{k}'}) m_0(E_{\boldsymbol{p}}) \boldsymbol{v}_{\boldsymbol{k}} \left(\boldsymbol{V}_{\boldsymbol{p}+\boldsymbol{k}-\boldsymbol{k}'} \cdot \boldsymbol{\nabla} \mu_m \tau_m\right). \quad \text{(S96)}$$

Equation (S96) can be simplified assuming that the magnon momentum $\boldsymbol{p}$ exceeds by far the momentum of exciton. Such a large-p/small-k asymptotics corresponds to the regime studied above in Sec. S7 B. Hence, in Eq. (S96) we decompose $\boldsymbol{V}_{\boldsymbol{p}+\boldsymbol{k}-\boldsymbol{k}'}$ in series over $|\boldsymbol{k}-\boldsymbol{k}'| \ll p$. Technically, it is convenient to introduce a novel variable $\boldsymbol{P} = \boldsymbol{p} + \boldsymbol{k} - \boldsymbol{k}'$, rewrite the sum as

$$\boldsymbol{v} = \frac{1}{\sum_{\boldsymbol{k}} f_0(\varepsilon_{\boldsymbol{k}})} \tau_p \frac{2\pi}{\hbar} \sum_{\boldsymbol{P},\boldsymbol{k},\boldsymbol{k}'} f_0'(\varepsilon_{\boldsymbol{k}}) |M(\boldsymbol{k},\boldsymbol{p};\boldsymbol{k}'-\boldsymbol{k})|^2 \delta(\varepsilon_{\boldsymbol{k}} - \varepsilon_{\boldsymbol{k}'}) m_0(E_{\boldsymbol{P}+\boldsymbol{k}'-\boldsymbol{k}}) \boldsymbol{v}_{\boldsymbol{k}} \left(\boldsymbol{V}_{\boldsymbol{P}} \cdot \boldsymbol{\nabla} \mu_m \tau_m\right)$$
$$= \frac{1}{\sum_{\boldsymbol{k}} f_0(\varepsilon_{\boldsymbol{k}})} \tau_p \frac{2\pi}{\hbar} \sum_{\boldsymbol{P},\boldsymbol{k},\boldsymbol{k}'} f_0'(\varepsilon_{\boldsymbol{k}}) |M(\boldsymbol{k},\boldsymbol{p};\boldsymbol{k}'-\boldsymbol{k})|^2 \delta(\varepsilon_{\boldsymbol{k}} - \varepsilon_{\boldsymbol{k}'}) m_0'(E_{\boldsymbol{P}}) \hbar [(\boldsymbol{k}'-\boldsymbol{k})\boldsymbol{V}_{\boldsymbol{P}}] \boldsymbol{v}_{\boldsymbol{k}} \left(\boldsymbol{V}_{\boldsymbol{P}} \cdot \boldsymbol{\nabla} \mu_m \tau_m\right). \quad \text{(S97)}$$

This expression can be brought to the form similar to Eq. (S84):

$$\boldsymbol{v} = \tau_p \Gamma^m \boldsymbol{u} = \frac{\Gamma^m}{\Gamma^0 + \Gamma^m} \boldsymbol{u}, \quad \text{(S98)}$$

where the magnon velocity $\boldsymbol{u}$ is defined in Eq. (S93). Note that in this approximation

$$\delta f(\boldsymbol{k}) = \tau_p \times \frac{2\pi}{\hbar} f_0'(\varepsilon_{\boldsymbol{k}}) \sum_{\boldsymbol{p},\boldsymbol{k}'} |M(\boldsymbol{k},\boldsymbol{p};\boldsymbol{k}'-\boldsymbol{k})|^2 \delta(\varepsilon_{\boldsymbol{k}} - \varepsilon_{\boldsymbol{k}'}) m_0'(E_{\boldsymbol{p}}) \hbar [(\boldsymbol{k}'-\boldsymbol{k})\boldsymbol{V}_{\boldsymbol{p}}] \left(\boldsymbol{V}_{\boldsymbol{p}} \cdot \boldsymbol{\nabla} \mu_m \tau_m\right)$$
$$= \tau_p \times (-\boldsymbol{k}) f_0'(\varepsilon_{\boldsymbol{k}}) \frac{2\pi}{\hbar} \underbrace{\sum_{\boldsymbol{k}'} |M(\boldsymbol{k},\boldsymbol{p};\boldsymbol{k}'-\boldsymbol{k})|^2 \delta(\varepsilon_{\boldsymbol{k}} - \varepsilon_{\boldsymbol{k}'}) (1 - \cos\vartheta_{\boldsymbol{k},\boldsymbol{k}'})}_{\Gamma^m / \sum_{\boldsymbol{p}} m_0(E_{\boldsymbol{p}})}$$
$$\times \underbrace{\sum_{\boldsymbol{p}} \tau_m m_0'(E_{\boldsymbol{p}}) \boldsymbol{V}_{\boldsymbol{p}} [\boldsymbol{V}_{\boldsymbol{p}} \boldsymbol{\nabla} \mu_m]}_{\boldsymbol{u} \sum_{\boldsymbol{p}} m_0(E_{\boldsymbol{p}})}. \quad \text{(S99)}$$

Let us now analyze the non-equilibrium exciton distribution function and drift velocity depending on the properties of exciton-magnon interaction. To that end, let us consider a simple one-dimensional version of the model above which simplifies the calculations and allows us to present the results for the distribution function in a simple analytical form. We note that the energy conservation law $\varepsilon_k = \varepsilon_{k'}$ provides two solutions: (i) $k' = k$ and (ii) $k' = -k$. The first solution does not provide any contribution to $\delta f(k)$ in Eq. (S95) after summation over p since V_p

is an odd function of p. The remaining contribution simplifies to

$$\delta f(\boldsymbol{k}) = \tau_p \times \frac{2\pi}{\hbar} f_0'(\varepsilon_k) \sum_{p,k'} |M(k,p;k'-k)|^2 \delta(\varepsilon_k - \varepsilon_{k'}) m_0(E_p) \left(V_{p+k-k'} \cdot \nabla \mu_m \tau_m\right). \tag{S100}$$

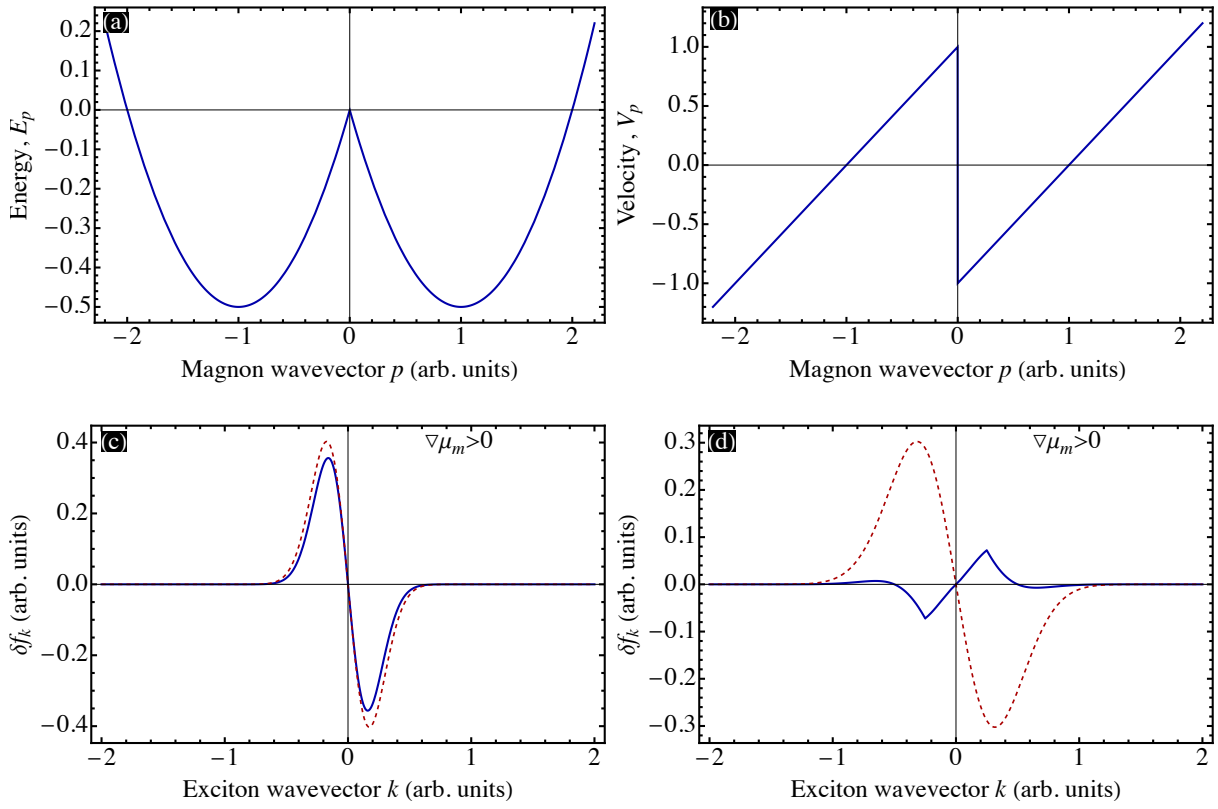

Supplementary Figure 13. 1D toy model. (a) Magnon dispersion $E_p = -\alpha|p| + p^2/2M_m$. (b) Magnon group velocity. (c,d) Anisotropic part of exciton distribution δf_k [blue solid curve, up to a positive prefactor] found numerically from Eq. (S100) (solid curve) and using the small-k asymptotics [red dotted curve, cf. Eq. (S99)]. Exciton dispersion $\varepsilon_k = \hbar^2 k^2/2M_x$. We use the dimensionless parameters $\alpha = 1$, $M_m = 1$, $M_x/M_m = 0.1$, $T = 0.3$. No cut-off ($p_0 \to \infty$) in (c). Cut-off parameter $p_0 = 0.5$ in (d).

Figure **13** shows the toy model dispersion of magnons (a), their group velocity (b) and the exciton distribution function found numerically from (S100) (c,d) for two models of interaction. For panel (c) we consider momentum independent matrix element M. For panel (d) we consider a more general case with the cut-off momentum p_0:

$$M(k,p,q) = \begin{cases} M, & p < p_0, \\ 0, & p \geqslant p_0. \end{cases} \tag{S101}$$

In this model the interaction with magnons with large momenta is absent. The result of numerical calculation of $\delta f(k)$ after Eq. (S100) is shown in Fig. **13**(d). In contrast to Fig. **13**(c) [and large

p/small k asymptotics (S99) shown by the dashed curve] here the occupancies of excitons with $k > 0$ are higher than those with $k < 0$ and excitons flow counter to the magnon flux $\boldsymbol{v} \uparrow\downarrow \boldsymbol{u}$. The situation shown in panel (d) corresponds to the negative drag of excitons by magnons with

$$\boldsymbol{v} \uparrow\downarrow \boldsymbol{u}.$$

S8. EMISSION DYNAMICS AT DIFFERENT ENERGIES IN THE 10L CRYSTAL.

We measured the spectrally dispersed PL decay of our 10L crystal at low temperature where spectral features are well resolved. The color-coded rectangles superimposed on the time-integrated PL spectrum Fig. **14**a indicate the respective spectral positions of the PL decay curves in **b** extracted from the Streak camera image. A single exponential fit shows that all four PL decay curves are essentially characterized by the same lifetime ($\tau = (12 \pm 1)\, ps$). It does not depend on the emission energy and is the same whether we analyze the X_0 peak or any of the other low-energy peaks. These results therefore complement our analysis shown in Extended Data Fig. 1: Whether we isolate the X_0 emission peak or integrate over all low-energy emissions and the X_0 peak, the spatio-temporal dynamics and the extracted diffusion coefficients are essentially the same.

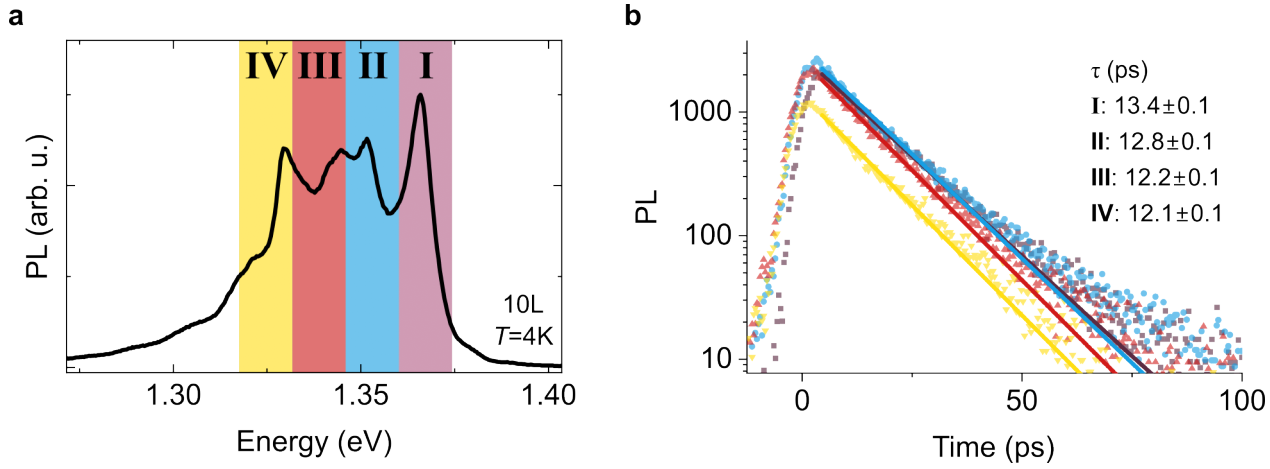

Supplementary Figure 14. **Emission dynamics at different energies in the 10L PL signal.** **a** Time-integrated PL emission spectrum. **b** PL decay curves extracted from a spectrally resolved Streak camera measurement at the energy windows color-coded in a. Laser excitation fluence was 490 µJ/cm^2 and the sample temperature $T = 4\,\mathrm{K}$ for all measurements.

S9. SIZE OF THE ZERO-DELAY PL EMISSION SPOT.

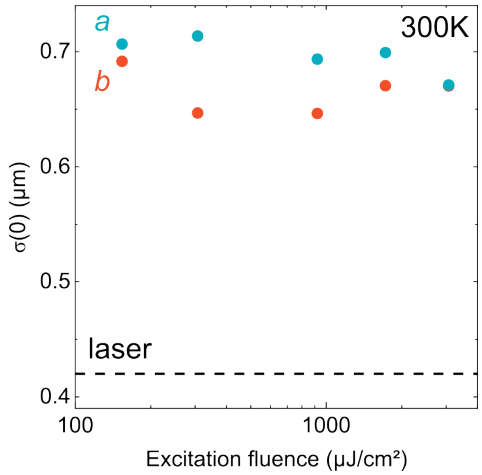

Supplementary Figure 15. Variance of the PL emission profile collected for four picoseconds. Data is shown for different crystallographic axes and excitation fluences. The width of the laser imaged on the Streak camera is indicated by the black dashed line.

S10. TEMPERATURE DEPENDENCE OF EXCITON LIFETIMES

Here, we briefly discuss the anomalous temperature dependence of the exciton lifetime shown in Extended Data Fig. 3b. In most materials, the emission lifetime of excitons tends to decrease with increasing temperatures, mainly due to faster, temperature-activated non-radiative recombination channels. Interestingly, in an ideal semiconductor quantum well with intrinsic radiative recombination, the lifetime is in fact expected to increase with temperature [78], as the excitonic distribution spreads out in momentum space, which reduces the fraction of excitons with momenta inside the light cone. Similar behavior is predicted for 2D semiconductors, with values in the range of 10's to 100's of ps for monolayer transition-metal dichalcogenides in the similar temperature range [79].

For the magnetic semiconductor CrSBr, additional effects may be considered. A recent spectroscopy study reports an anomalous temperature dependent reduction of the exciton oscillator strength [80]. The oscillator strength is observed to sizably decrease as a function of temperature, an unusual behavior when compared to Wannier-Mott excitons in other inorganic semiconductors. Calculations based on ab-initio many-body perturbation theory suggest an intriguing microscopic reason for this peculiar change in oscillator strength, which is related to the presence of spin fluctuations. Spin disorder modifies the orbital composition of the exciton wave function. More specifically, it quenches the inter-site contribution, i.e., the hopping of electrons and holes between neighboring Cr-atoms, which is to a large extent responsible for the large oscillator strength of excitons in CrSBr. Phenomenologically, it can be argued that magnetic disorder, by reducing inter-site hopping, leads to a decrease of the exciton oscillator strength, and, as a results, to an increase of the radiative lifetime of excitons. If the decay of the exciton population observed in our experiments is indeed limited by radiative recombination, this effect could qualitatively explain the peculiar dependence of the exciton lifetime in Extended Data Fig. 3b.

[1] Kyle L Seyler, Ding Zhong, Dahlia R Klein, Shiyuan Gao, Xiaoou Zhang, Bevin Huang, Efrén Navarro-Moratalla, Li Yang, David H Cobden, Michael A McGuire, *et al.*, "Ligand-field helical luminescence in a 2D ferromagnetic insulator," Nature Physics **14**, 277–281 (2018).

[2] Zhaowei Zhang, Jingzhi Shang, Chongyun Jiang, Abdullah Rasmita, Weibo Gao, and Ting Yu, "Direct photoluminescence probing of ferromagnetism in monolayer two-dimensional $CrBr_3$," Nano Letters **19**, 3138–3142 (2019).

[3] Soonmin Kang, Kangwon Kim, Beom Hyun Kim, Jonghyeon Kim, Kyung Ik Sim, Jae-Ung Lee, Sungmin Lee, Kisoo Park, Seokhwan Yun, Taehun Kim, *et al.*, "Coherent many-body exciton in van der Waals antiferromagnet $NiPS_3$," Nature **583**, 785–789 (2020).

[4] Nathan P. Wilson, Kihong Lee, John Cenker, Kaichen Xie, Avalon H. Dismukes, Evan J. Telford, Jordan Fonseca, Shivesh Sivakumar, Cory Dean, Ting Cao, Xavier Roy, Xiaodong Xu, and Xiaoyang Zhu, "Interlayer electronic coupling on demand in a 2D magnetic semiconductor," Nature Materials **20**, 1675 (2021).

[5] Mario Norberto Baibich, Jean Marc Broto, Albert Fert, F Nguyen Van Dau, Frédéric Petroff, P Etienne, G Creuzet, A Friederich, and J Chazelas, "Giant magnetoresistance of (001) Fe/(001) Cr magnetic superlattices," Physical Review Letters **61**, 2472 (1988).

[6] Grünberg Binasch, Peter Grünberg, F Saurenbach, and W Zinn, "Enhanced magnetoresistance in layered magnetic structures with antiferromagnetic interlayer exchange," Physical Review B **39**, 4828 (1989).

[7] Youn Jue Bae, Jue Wang, Allen Scheie, Junwen Xu, Daniel G Chica, Geoffrey M Diederich, John Cenker, Michael E Ziebel, Yusong Bai, Haowen Ren, *et al.*, "Exciton-coupled coherent magnons in a 2D semiconductor," Nature **609**, 282–286 (2022).

[8] Geoffrey M Diederich, John Cenker, Yafei Ren, Jordan Fonseca, Daniel G Chica, Youn Jue Bae, Xiaoyang Zhu, Xavier Roy, Ting Cao, Di Xiao, *et al.*, "Tunable interaction between excitons and hybridized magnons in a layered semiconductor," Nature Nanotechnology **18**, 23–28 (2023).

[9] Florian Dirnberger, Jiamin Quan, Rezlind Bushati, Geoffrey M Diederich, Matthias Florian, Julian Klein, Kseniia Mosina, Zdenek Sofer, Xiaodong Xu, Akashdeep Kamra, *et al.*, "Magneto-optics in a van der Waals magnet tuned by self-hybridized polaritons," Nature **620**, 533–537 (2023).

[10] Dmitrii Unuchek, Alberto Ciarrocchi, Ahmet Avsar, Kenji Watanabe, Takashi Taniguchi, and Andras

Kis, "Room-temperature electrical control of exciton flux in a van der Waals heterostructure," Nature **560**, 340–344 (2018).

[11] Yinan Dong, Lin Xiong, IY Phinney, Zhiyuan Sun, Ran Jing, AS McLeod, Shuai Zhang, Song Liu, FL Ruta, H Gao, *et al.*, "Fizeau drag in graphene plasmonics," Nature **594**, 513–516 (2021).

[12] Jakhangirkhodja A. Tulyagankhodjaev, Petra Shih, Jessica Yu, Jake C. Russell, Daniel G. Chica, Michelle E. Reynoso, Haowen Su, Athena C. Stenor, Xavier Roy, Timothy C. Berkelbach, and Milan Delor, "Room-temperature wavelike exciton transport in a van der Waals superatomic semiconductor," Science **382**, 438–442 (2023).

[13] Magdalena Birowska, Paulo E Faria Junior, Jaroslav Fabian, and Jens Kunstmann, "Large exciton binding energies in $MnPS_3$ as a case study of a van der Waals layered magnet," Physical Review B **103**, L121108 (2021).

[14] Suhyeon Kim, Sangho Yoon, Hyobin Ahn, Gangtae Jin, Hyesun Kim, Moon-Ho Jo, Changgu Lee, Jonghwan Kim, and Sunmin Ryu, "Photoluminescence path bifurcations by spin flip in two-dimensional $CrPS_4$," ACS Nano **16**, 16385–16393 (2022).

[15] Anjan Barman, Gianluca Gubbiotti, Sam Ladak, Adekunle Olusola Adeyeye, Maciej Krawczyk, Joachim Gräfe, Christoph Adelmann, Sorin Cotofana, Azad Naeemi, Vitaliy I Vasyuchka, *et al.*, "The 2021 magnonics roadmap," Journal of Physics: Condensed Matter **33**, 413001 (2021).

[16] R Lebrun, A Ross, SA Bender, A Qaiumzadeh, L Baldrati, J Cramer, A Brataas, RA Duine, and M Kläui, "Tunable long-distance spin transport in a crystalline antiferromagnetic iron oxide," Nature **561**, 222–225 (2018).

[17] Sa Tu, Timothy Ziman, Guoqiang Yu, Caihua Wan, Junfeng Hu, Hao Wu, Hanchen Wang, Mengchao Liu, Chuanpu Liu, Chenyang Guo, *et al.*, "Record thermopower found in an irmn-based spintronic stack," Nature communications **11**, 2023 (2020).

[18] Kyusup Lee, Dong-Kyu Lee, Dongsheng Yang, Rahul Mishra, Dong-Jun Kim, Sheng Liu, Qihua Xiong, Se Kwon Kim, Kyung-Jin Lee, and Hyunsoo Yang, "Superluminal-like magnon propagation in antiferromagnetic NiO at nanoscale distances," Nature Nanotechnology **16**, 1337–1341 (2021).

[19] JR Hortensius, D Afanasiev, M Matthiesen, R Leenders, R Citro, AV Kimel, RV Mikhaylovskiy, BA Ivanov, and AD Caviglia, "Coherent spin-wave transport in an antiferromagnet," Nature Physics **17**, 1001–1006 (2021).

[20] X-Y Wei, O Alves Santos, CH Sumba Lusero, GEW Bauer, J Ben Youssef, and BJ van Wees, "Giant magnon spin conductivity in ultrathin yttrium iron garnet films," Nature Materials **21**, 1352–1356

(2022).

[21] Yue Sun, Fanhao Meng, Changmin Lee, Aljoscha Soll, Hongrui Zhang, Ramamoorthy Ramesh, Jie Yao, Zdeněk Sofer, and Joseph Orenstein, "Dipolar spin wave packet transport in a van der Waals antiferromagnet," Nature Physics , 1–7 (2024).

[22] O Göser, W Paul, and HG Kahle, "Magnetic properties of CrSBr," Journal of Magnetism and Magnetic Materials **92**, 129–136 (1990).

[23] Evan J Telford, Avalon H Dismukes, Kihong Lee, Minghao Cheng, Andrew Wieteska, Amymarie K Bartholomew, Yu-Sheng Chen, Xiaodong Xu, Abhay N Pasupathy, Xiaoyang Zhu, *et al.*, "Layered antiferromagnetism induces large negative magnetoresistance in the van der Waals semiconductor CrSBr," Advanced Materials **32**, 2003240 (2020).

[24] Fangchao Long, Kseniia Mosina, René Hübner, Zdenek Sofer, Julian Klein, Slawomir Prucnal, Manfred Helm, Florian Dirnberger, and Shengqiang Zhou, "Intrinsic magnetic properties of the layered antiferromagnet CrSBr," Applied Physics Letters **123** (2023).

[25] Alessandra Canetta, Serhii Volosheniuk, Sayooj Satheesh, José Pedro Alvarinhas Batista, Aloïs Castellano, Riccardo Conte, Daniel G Chica, Kenji Watanabe, Takashi Taniguchi, Xavier Roy, *et al.*, "Impact of spin-entropy on the thermoelectric properties of a 2D magnet," arXiv:2403.08581 (2024).

[26] Julian Klein, Benjamin Pingault, Matthias Florian, Marie-Christin Heißenbüttel, Alexander Steinhoff, Zhigang Song, Kierstin Torres, Florian Dirnberger, Jonathan B Curtis, Mads Weile, *et al.*, "The bulk van der Waals layered magnet CrSBr is a quasi-1D material," ACS Nano **17**, 5316–5328 (2023).

[27] Farsane Tabataba-Vakili, Huy PG Nguyen, Anna Rupp, Kseniia Mosina, Anastasios Papavasileiou, Kenji Watanabe, Takashi Taniguchi, Patrick Maletinsky, Mikhail M Glazov, Zdenek Sofer, *et al.*, "Doping-control of excitons and magnetism in few-layer CrSBr," arXiv:2312.11041 (2023).

[28] Christian Meineke, Jakob Schlosser, Martin Zizlsperger, Marlene Liebich, Niloufar Nilforoushan, Kseniia Mosina, Sophia Terres, Alexey Chernikov, Zdenek Sofer, Markus A Huber, *et al.*, "Ultrafast exciton dynamics in the atomically thin van der Waals magnet CrSBr," Nano Letters (2024).

[29] Kaiman Lin, Xiaoxiao Sun, Florian Dirnberger, Yi Li, Jiang Qu, Peiting Wen, Zdenek Sofer, Aljoscha Söll, Stephan Winnerl, Manfred Helm, Shengqiang Zhou, Yaping Dan, and Slawomir Prucnal, "Strong Exciton–Phonon Coupling as a Fingerprint of Magnetic Ordering in van der Waals Layered CrSBr," ACS Nano **18**, 2898–2905 (2024).

[30] Marvin Kulig, Jonas Zipfel, Philipp Nagler, Sofia Blanter, Christian Schüller, Tobias Korn, Nicola Paradiso, Mikhail M. M. Glazov, and Alexey Chernikov, "Exciton Diffusion and Halo Effects in

Monolayer Semiconductors," Physical Review Letters **120**, 207401 (2018).

[31] Naomi S Ginsberg and William A Tisdale, "Spatially resolved photogenerated exciton and charge transport in emerging semiconductors," Annual Review of Physical Chemistry **71**, 1–30 (2020).

[32] Marco Bianchi, Swagata Acharya, Florian Dirnberger, Julian Klein, Dimitar Pashov, Kseniia Mosina, Zdenek Sofer, Alexander N Rudenko, Mikhail I Katsnelson, Mark van Schilfgaarde, *et al.*, "Paramagnetic electronic structure of CrSBr: Comparison between ab initio GW theory and angle-resolved photoemission spectroscopy," Physical Review B **107**, 235107 (2023).

[33] Marco Bianchi, Kimberly Hsieh, Esben Juel Porat, Florian Dirnberger, Julian Klein, Kseniia Mosina, Zdenek Sofer, Alexander N Rudenko, Mikhail I Katsnelson, Yong P Chen, *et al.*, "Charge transfer induced Lifshitz transition and magnetic symmetry breaking in ultrathin CrSBr crystals," Physical Review B **108**, 195410 (2023).

[34] Fan Wu, Ignacio Gutiérrez-Lezama, Sara A López-Paz, Marco Gibertini, Kenji Watanabe, Takashi Taniguchi, Fabian O von Rohr, Nicolas Ubrig, and Alberto F Morpurgo, "Quasi-1D electronic transport in a 2D magnetic semiconductor," Advanced Materials **34**, 2109759 (2022).

[35] XP Vögele, D Schuh, W Wegscheider, JP Kotthaus, and AW Holleitner, "Density enhanced diffusion of dipolar excitons within a one-dimensional channel," Physical Review Letters **103**, 126402 (2009).

[36] Nardeep Kumar, Qiannan Cui, Frank Ceballos, Dawei He, Yongsheng Wang, and Hui Zhao, "Exciton-exciton annihilation in $MoSe_2$ monolayers," Physical Review B **89**, 125427 (2014).

[37] Andrei Kirilyuk, Alexey V Kimel, and Theo Rasing, "Ultrafast optical manipulation of magnetic order," Reviews of Modern Physics **82**, 2731 (2010).

[38] Y Au, Mykola Dvornik, T Davison, E Ahmad, Paul Steven Keatley, Arne Vansteenkiste, Bartel Van Waeyenberge, and VV Kruglyak, "Direct excitation of propagating spin waves by focused ultrashort optical pulses," Physical Review Letters **110**, 097201 (2013).

[39] Kyongmo An, Kevin S Olsson, Annie Weathers, Sean Sullivan, Xi Chen, Xiang Li, Luke G Marshall, Xin Ma, Nikita Klimovich, Jianshi Zhou, *et al.*, "Magnons and phonons optically driven out of local equilibrium in a magnetic insulator," Physical Review Letters **117**, 107202 (2016).

[40] Raül Perea-Causín, Samuel Brem, Roberto Rosati, Roland Jago, Marvin Kulig, Jonas D. Ziegler, Jonas Zipfel, Alexey Chernikov, and Ermin Malic, "Exciton propagation and halo formation in two-dimensional materials," Nano Letters **19**, 7317–7323 (2019).

[41] A. E. Bulatov and S. G. Tikhodeev, "Phonon-driven carrier transport caused by short excitation pulses in semiconductors," Physical Review B **46**, 15058–15062 (1992).

[42] M. M. Glazov, "Phonon wind and drag of excitons in monolayer semiconductors," Physical Review B **100**, 045426 (2019).

[43] FJ Blatt, DJ Flood, V Rowe, PA Schroeder, and JE Cox, "Magnon-drag thermopower in iron," Physical Review Letters **18**, 395 (1967).

[44] Zhiyong Qiu, Jia Li, Dazhi Hou, Elke Arenholz, Alpha T N'Diaye, Ali Tan, Ken-ichi Uchida, Koji Sato, Satoshi Okamoto, Yaroslav Tserkovnyak, *et al.*, "Spin-current probe for phase transition in an insulator," Nature Communications **7**, 12670 (2016).

[45] Junxue Li, Zhong Shi, Victor H Ortiz, Mohammed Aldosary, Cliff Chen, Vivek Aji, Peng Wei, and Jing Shi, "Spin Seebeck effect from antiferromagnetic magnons and critical spin fluctuations in epitaxial FeF_2 films," Physical Review Letters **122**, 217204 (2019).

[46] Yuanhua Zheng, Tianqi Lu, Md MH Polash, Morteza Rasoulianboroujeni, Ning Liu, Michael E Manley, Yuan Deng, PJ Sun, XL Chen, Raphael P Hermann, *et al.*, "Paramagnon drag in high thermoelectric figure of merit Li-doped MnTe," Science Advances **5**, eaat9461 (2019).

[47] Jonas D. Ziegler, Jonas Zipfel, Barbara Meisinger, Matan Menahem, Xiangzhou Zhu, Takashi Taniguchi, Kenji Watanabe, Omer Yaffe, David A. Egger, and Alexey Chernikov, "Fast and anomalous exciton diffusion in two-dimensional hybrid perovskites," Nano Letters **20**, 6674–6681 (2020).

[48] D. Beret, L. Ren, C. Robert, L. Foussat, P. Renucci, D. Lagarde, A. Balocchi, T. Amand, B. Urbaszek, K. Watanabe, T. Taniguchi, X. Marie, and L. Lombez, "Nonlinear diffusion of negatively charged excitons in monolayer WSe_2," Physical Review B **107**, 045420 (2023).

[49] Y-J Chen, Kh Zakeri, A Ernst, HJ Qin, Y Meng, and J Kirschner, "Group velocity engineering of confined ultrafast magnons," Physical Review Letters **119**, 267201 (2017).

[50] Chen Ye, Cong Wang, Qiong Wu, Sheng Liu, Jiayuan Zhou, Guopeng Wang, Aljoscha Soll, Zdenek Sofer, Ming Yue, Xue Liu, *et al.*, "Layer-dependent interlayer antiferromagnetic spin reorientation in air-stable semiconductor CrSBr," ACS Nano **16**, 11876–11883 (2022).

[51] Huicong Liu and Ka Shen, "Spin wave dynamics excited by a focused laser pulse in antiferromagnet CrSBr," Physical Review B **110**, 024424 (2024).

[52] Youn Jue Bae, Taketo Handa, Yanan Dai, Jue Wang, Huicong Liu, Allen Scheie, Daniel G Chica, Michael E Ziebel, Andrew D Kent, Xiaodong Xu, *et al.*, "Transient magnetoelastic coupling in CrSBr," Physical Review B **109**, 104401 (2024).

[53] Evan J Telford, Avalon H Dismukes, Raymond L Dudley, Ren A Wiscons, Kihong Lee, Daniel G Chica, Michael E Ziebel, Myung-Geun Han, Jessica Yu, Sara Shabani, *et al.*, "Coupling between magnetic

order and charge transport in a two-dimensional magnetic semiconductor," Nature Materials **21**, 754–760 (2022).

[54] Shane Smolenski, Ming Wen, Qiuyang Li, Eoghan Downey, Adam Alfrey, Wenhao Liu, Aswin LN Kondusamy, Aaron Bostwick, Chris Jozwiak, Eli Rotenberg, *et al.*, "Large exciton binding energy in the bulk van der waals magnet crsbr," arXiv:2403.13897 (2024).

[55] Qiuyang Li, Xin Xie, Adam Alfrey, Christiano W Beach, Nicholas McLellan, Yang Lu, Jiaqi Hu, Wenhao Liu, Nikhil Dhale, Bing Lv, *et al.*, "Magnetic exciton-polariton with strongly coupled atomic and photonic anisotropies," arXiv:2306.11265 (2023).

[56] Alexey Chernikov and Mikhail M. Glazov, "Chapter three - exciton diffusion in 2D van der waals semiconductors," in *Semiconductors and Semimetals*, Vol. 112, edited by Parag B. Deotare and Zetian Mi (Elsevier, 2023) pp. 69–110.

[57] M. M. Glazov, Z. A. Iakovlev, and S. Refaely-Abramson, "Phonon-induced exciton weak localization in two-dimensional semiconductors," Applied Physics Letters **121**, 192106 (2022).

[58] Koloman Wagner, Jonas Zipfel, Roberto Rosati, Edith Wietek, Jonas D Ziegler, Samuel Brem, Raül Perea-Causín, Takashi Taniguchi, Kenji Watanabe, Mikhail M Glazov, *et al.*, "Nonclassical exciton diffusion in monolayer WSe_2," Physical Review Letters **127**, 076801 (2021).

[59] Shinichiro Mouri, Yuhei Miyauchi, Minglin Toh, Weijie Zhao, Goki Eda, and Kazunari Matsuda, "Nonlinear photoluminescence in atomically thin layered WSe_2 arising from diffusion-assisted exciton-exciton annihilation," Physical Review B **90**, 155449 (2014).

[60] Dezheng Sun, Yi Rao, Georg A Reider, Gugang Chen, Yumeng You, Louis Brézin, Avetik R Harutyunyan, and Tony F Heinz, "Observation of rapid exciton–exciton annihilation in monolayer molybdenum disulfide," Nano letters **14**, 5625–5629 (2014).

[61] Long Yuan, Ti Wang, Tong Zhu, Mingwei Zhou, and Libai Huang, "Exciton dynamics, transport, and annihilation in atomically thin two-dimensional semiconductors," The journal of physical chemistry letters **8**, 3371–3379 (2017).

[62] Edith Wietek, Matthias Florian, Jonas Göser, Takashi Taniguchi, Kenji Watanabe, Alexander Högele, Mikhail M. Glazov, Alexander Steinhoff, and Alexey Chernikov, "Nonlinear and negative effective diffusivity of interlayer excitons in moiré-free heterobilayers," Phys. Rev. Lett. **132**, 016202 (2024).

[63] Jonas Zipfel, Marvin Kulig, Raül Perea-Causín, Samuel Brem, Jonas D Ziegler, Roberto Rosati, Takashi Taniguchi, Kenji Watanabe, Mikhail M Glazov, Ermin Malic, *et al.*, "Exciton diffusion in monolayer semiconductors with suppressed disorder," Physical Review B **101**, 115430 (2020).

[64] AJ Goodman, D-H Lien, GH Ahn, LL Spiegel, M Amani, AP Willard, A Javey, and WA Tisdale, "Substrate-dependent exciton diffusion and annihilation in chemically treated mos2 and ws2," The Journal of Physical Chemistry C **124**, 12175–12184 (2020).

[65] Conyers Herring and Erich Vogt, "Transport and deformation-potential theory for many-valley semiconductors with anisotropic scattering," Phys. Rev. **101**, 944–961 (1956).

[66] V. F. Gantmakher and Y .B. Levinson, *Carrier Scattering in Metals and Semiconductors* (North-Holland Publishing Company, 1987).

[67] L.D. Landau and E.M. Lifshitz, *The Classical Theory of Fields* (Butterworth-Heinemann, Oxford, 1975).

[68] M.M. Glazov, *Electron & Nuclear Spin Dynamics in Semiconductor Nanostructures*, Series on Semiconductor Science and Technology (OUP Oxford, 2018).

[69] Allen Scheie, Michael Ziebel, Daniel G. Chica, Youn June Bae, Xiaoping Wang, Alexander I. Kolesnikov, Xiaoyang Zhu, and Xavier Roy, "Spin waves and magnetic exchange hamiltonian in CrSBr," Advanced Science **9**, 2202467 (2022).

[70] E. M. Lifshitz and L. P. Pitaevskii, *Statistical Physics: Theory of the Condensed State* (Butterworth-Heinemann, Oxford, 2002).

[71] A. I. Akhiezer, V. G. Bariakhtar, and S. V. Peletminskiĭ, *Spin Waves*, North-Holland series in low temperature physics (North-Holland Publishing Company, 1968).

[72] Alexander G Gurevich and Gennadii A Melkov, *Magnetization oscillations and waves* (CRC press, 2020).

[73] Frederic Keffer, "Spin waves," in *Ferromagnetism / Ferromagnetismus*, edited by H. P. J. Wijn (Springer Berlin Heidelberg, Berlin, Heidelberg, 1966) pp. 1–273.

[74] L. V. Keldysh, "Phonon wind and dimensions of electron-hole drops in semiconductors," JETP Lett. **23**, 86 (1976).

[75] N. N. Zinov'ev, L.P. Ivanov, V.I. Kozub, and I.D. Yaroshetskii, "Exciton transport by nonequllibrium phonons and its effect on recombination radiation from semiconductors at high excitation levels," JETP **57**, 1027 (1983).

[76] G. A. Kopelevich, S. G. Tikhodeev, and N. A. Gippius, "Phonon wind and excitonic transport in Cu_2O semiconductors," Soviet Journal of Experimental and Theoretical Physics **82**, 1180–1185 (1996).

[77] S. G. Tikhodeev, G. A. Kopelevich, and N. A. Gippius, "Exciton transport in Cu_2O: Phonon wind

versus superfluidity," physica status solidi (b) **206**, 45–53 (1998).

[78] Lucio Claudio Andreani, Francesco Tassone, and Franco Bassani, "Radiative lifetime of free excitons in quantum wells," Solid state communications **77**, 641–645 (1991).

[79] Haining Wang, Changjian Zhang, Weimin Chan, Christina Manolatou, Sandip Tiwari, and Farhan Rana, "Radiative lifetimes of excitons and trions in monolayers of the metal dichalcogenide mos 2," Physical Review B **93**, 045407 (2016).

[80] Yinming Shao, Florian Dirnberger, Siyuan Qiu, Swagata Acharya, Sophia Terres, Evan J Telford, Dimitar Pashov, Brian SY Kim, Francesco L Ruta, Daniel G Chica, *et al.*, "Magnetically confined surface and bulk excitons in a layered antiferromagnet," Nature Materials , 1–8 (2025).